INVESTIGATION OF ACCURACY IN QUANTITATION OF ^{18}F-FDG CONCENTRATION OF PET/CT

A Thesis

Submitted to the Graduate Faculty of the
Louisiana State University and
Agricultural and Mechanical College
in partial fulfillment of the
requirements for the degree of
Master of Science

in

The Department of Physics and Astronomy

by
Yuri Ishihara
M.D., Mie University School of Medicine, 1993
December 2004

Acknowledgements

I would like to acknowledge the support and guidance of Dr. Steven Bujenovic, my advisor at the Lake PET Imaging Center. He introduced me to this fascinating field of medical imaging in clinical settings. He always was available to answer my questions. He was a great teacher who always emphasized critical thinking and encouraged my research, even when I had a hard time.

I cannot forget to thank to Ranjit Chakrabarti and Ryan Wagley, technologists at the Lake PET Imaging Center who were very patient with me in assisting in the operation of the scanners. Many thanks to all the staff who created a great atmosphere to work in. Without their help, I could not acquire imaging data for my thesis.

The guidance of Dr. Kenneth Matthews, my advisor at LSU was invaluable. He was always willing to answer my numerous questions in nuclear medicine during his busy hours. Discussion with him about a medical physics career was invaluable and his guidance in the medical imaging field was unforgettable.

Thanks to Dr. Erno Sajo who gave me excellent technical advice and encouragement throughout my medical physics study. He also generously gave me permission to use his equipment. Not only being a very intelligent scientist, but also being a truly considerate person, he gave me encouragement to complete my graduate study.

I also thank Dr. Oscar Hidalgo and Dr. Sheldon Johnson for their support during my rotation at the Mary Bird Perkins Cancer Center (MBPCC).

Thanks to Rajesh Manoharan, another graduate student who worked at the PET center with me. He was not only helpful to me in acquiring PET data but also helped me in many ways, especially during the last semester of my rotation at the MBPCC.

Many people have encouraged and helped me to continue my graduate study at Louisiana State University and the MBPCC. Only a few names have been mentioned here.

I thank Michael Domingue, my husband, for his great patience and support during my graduate study.

Finally, I am grateful for the financial support of Louisiana State University Board of Regents, providing my graduate fellowship.

Table of Contents

Abstract

The PET/CT scanner has been recognized as a powerful diagnostic imaging modality in oncology and radiation treatment planning. Traditionally, PET has been used for quantitative analysis, and diagnostic interpretations of PET images greatly relied on a nuclear medicine physician's experience and knowledge. The PET data set represents a positron emitter's activity concentration as a gray scale in each pixel. The assurance of the quantitative accuracy of the PET data is critical for diagnosis and staging of disease and evaluation of treatment. The standard uptake value (SUV) is a widely employed parameter in clinical settings to distinguish malignant lesions from others. SUV is a rough normalization of radioactive tracer uptake where normal tissue uptake is unity. The PET scanner is a sensitive diagnostic method to detect small lesions such as lymph node metastasis less than 1 cm in diameter, whereas the CT scanner may be limited in detecting these lesions. The accuracy of quantitation of small lesions is critical for predicting prognosis or planning a treatment of the patient. PET/CT uses attenuation correction factors obtained from CT scanner data sets. Non-biological materials such as metals and contrast agents are recognized as a factor that leads to a wrong scaling factor in the PET image. We challenge the accuracy of the quantitative method that physicians routinely use as a parameter to distinguish malignant lesions from others under clinical settings in commercially available CT/PET scanners. First, we verified if we could

recover constant activity concentration throughout the field of view for small identical activity concentration sources. Second, we tested how much the CT-based attenuation correction factor could be influenced by contrast agents. Third, we tested how much error in quantitation could be introduced by object size.

Our data suggest that the routine normalization process of the PET scanner does not guarantee an accurate quantitation of discrete uniform activity sources in the PET/CT scanner. Also, activity concentrations greatly rely on an object's dimensions and object size. A recovery correction factor is necessary on these quantitative data for oncological evaluation to assure accurate interpretation of the activity concentration. Development of parameters for quantitation other than SUV may overcome SUV's inherent limitations reflecting patient-specific physiology and the imaging characteristics of individual scanners.

Chapter 1

Introduction

1.1 Motivation

The hybrid system of a PET scanner combined with CT scanner (PET/CT) has gained popularity in the oncological community since its commercial introduction to the market in early 2001 [1]. The integrated PET/CT unit superimposes PET images on CT images with minimum co-registration problems between the two images by minimizing patient movement. Simultaneously providing anatomical information by CT scan helps physicians to identify the anatomical location of the lesion demonstrated on the PET images [2]. Integrated PET-CT has been shown to improve accuracy of the staging in cancers, such as lung cancer [3, 4] and head and neck cancer [5]. Another uniqueness of the PET/CT scanner is that the CT numbers gained from the CT data sets are converted into attenuation correction factors to correct images in the PET data sets.

Traditionally PET has been employed to differentiate benign lesions from malignant lesions and for staging of malignancy as a diagnostic modality [6-8]. Currently, the advantage of the PET/CT in radiation treatment planning (RTP) has been recognized because of its ability to demonstrate a tumor's physiological information. In RTP the target volumes are contoured and a dose is prescribed to these lesions. The PET/CT information potentially changes tumor target volume in the treatment planning [9]. Therefore, the quantitative accuracy of the PET/CT scanner is an issue.

2-deoxy-2-[^{18}F]-fluoro-D-glucose (^{18}F-FDG) PET/CT has been used as a radioactive tracer for imaging of brain, heart, and tumor diagnosis. ^{18}F-FDG is an analog of glucose (Figure 1-1). This tracer is injected into a patient intravenously and is transported into the cells mainly by the glucose transporters, GLUT1 and GLUT4 and phosphorylated by hexokinase, a rate limiting enzyme of glucose metabolism (Figure 1-2). ^{18}F-FDG-6-P, a phosporylated ^{18}F-FDG metabolite is negatively charged and cannot leave the cell, where it accumulates. With PET, we can visualize ^{18}F-FDG-6-P trapped into the cells of various tissues [10]. Cancer cells have a higher glycolysis rate compared to the tissue in which it arose. Increased ^{18}F-FDG uptake of the hypoxic cell reflects that these cells require more glucose uptake to support anaerobic glycolysis, mediated by an increase in expression of glucose transporters in the cell membrane. ^{18}F-FDG uptake does not directly reflect tumor-specific glucose metabolism.^{18}F-FDG uptake can occur in other glucose utilizing cells such as macrophages and leukocytes that are rich in inflammatory tissue and may cause a false positive study in PET. A recent histopathological study of ^{18}F-FDG uptake showed that ^{18}F-FDG is selectively demonstrated within viable and hypoxic cells *in vivo* [11]. This study indicates that PET has a potential to distinguish

hypoxic cell groups, which are more resistant to radiation therapy and more likely to be a source of distant metastasis or recurrence in the future. This suggests a unique role for PET in oncology treatment planning by distinguishing more resistant cell groups from the others; using PET for targeting with narrow beam intensity modulated radiation therapy can potentially deliver higher dose selectively to the more radiation resistant volume.

Imaging with ^{18}F-FDG is not the only radiopharmaceutical in the application of PET in oncology. 3'-deoxy-3'-[^{18}F] fluorothymidine (FLT) assesses tumor proliferation. FLT is uptaken by cells and phosphorylated by thymidine kinase 1. Images of FLT-monophosphate trapped in the cell reflect the thymidine kinase activity, which also is a measure of the rate of tumor proliferation. Knowledge of the patient's specific tumor proliferation potentially changes the fractionation schedule of radiation therapy [9].

One of the widely used quantitative parameter to distinguish malignant from benign lesions is standard uptake value (SUV), defined as:

$$SUV = \frac{Tracer\ uptake\,(MBq/mL)}{Administered\ activity\,(MBq)/(\,patient\ weight\,(kg)\times 1000)}. \quad (1)$$

The tracer does not distribute evenly throughout an entire patient's body. Normal SUV is by definition under this model roughly equal to one. Malignant lesions have higher glucose metabolic rates compared to the normal tissue with SUV's usually ranging from 4 to 15 [12]. A region of interest (ROI) is drawn by a physician and maximum, minimum, and average SUV are displayed on the image according to the software setting of the scanner. The maximum SUV particularly has diagnostic value, because (1) its value is independent of the lesion's area drawn by a person and (2) tumor lesions have heterogeneous SUV values, therefore we are most concerned with the highest metabolic rate.

Our question is: “How reliable are these SUV values?” PET scan images use gray scale maps to depict activity concentrations of a positron emitting source in the body. We decided to investigate major factors that can adversely alter SUV. The normalization process to an individual patient in Equation 1, where one divides by uniform distribution of the normal tissue, causes more error. Each individual has different metabolism of the tracer. Distributions of the activity concentration reflect an individual’s physiological function. Therefore, we ignored the denominator of Equation 1 and only concentrated on activity concentrations (the numerator) that are utilized to calculate SUV.

Many factors affect quantitative accuracy of the PET/CT; some are particularly unique to hybrid PET/CT scanners [1, 13, 14]. The scaling problem of attenuation values (μ) at 70 keV into 511 keV is an inherent problem for the PET/CT unit. The μ is an energy-dependent value. The attenuation correction factors are obtained from a CT scan at a mean energy of 70 keV and scaled into a μ at 511 keV by a manufacturer-dependent algorithm [1].

One problem is oral and intravenous iodinated contrast materials are commonly used in CT. They enhance attenuation in the gastrointestinal tract and in vessels to assist visual discrimination of these anatomic structures. This contrast can create artifacts in both the CT image and CT-based attenuation correction of the PET image [15-17].

Partial volume effect is another factor that affects quantitative analysis in PET. The volume of the object, relative to the spatial resolution of the imaging system, affects the recovery of activity concentration of PET and single photon emission computed tomography (SPECT). This effect has been discussed extensively for PET and SPECT brain research studies [18]. It is critical in a malignancy, such as glioblastoma

maltiforme, where a physician is interested in whether recurrent tumor is present compared to the normal cortex. We noticed that this partial volume effect of the PET/CT scanner is not widely considered when it comes to image interpretation in oncology settings.

Another issue that we did not cover in this thesis is organ movement. Physiological activity such as respiration, heart beat, and bowel movement are problematic [13, 19, 20]. Sometimes anatomical location of the lesion is disregarded because of artifacts created by physiological motion. Diagnosis of the patient with lesions at the base of the lung and the dome of the liver is particularly difficult. To solve respiratory motion, respiratory-gated PET scanning is under research development [21, 22].

Physicians are advised to review two sets of fused PET/CT images, using both attenuation corrected PET and non-attenuation corrected PET images [13]. One of the issues that PET/CT is facing is that this diagnostic area lies at the interaction of nuclear medicine physicians, radiologists, and radiation oncologists. Well-trained nuclear medicine physicians can make reasonable judgments whether a lesion is malignant or not from these two sets of data. However, most manufacturers do not routinely fuse non-attenuation corrected PET images to CT image data sets.

A goal is to use PET/CT scanners as a method of quantitative evaluation reflecting the biological behavior of the tumor. The accuracy of these quantitative values is critical to the target. A decision made about a patient's treatment causes tremendous effects on his or her quality of life. We were very curious in the clinical setting if the default PET/CT image reconstructions were sufficient to overcome attenuation correction

artifacts mentioned above and also the partial volume effects. Further, we search to understand the limitations of PET/CT in the clinical settings.

1.2 Organization of the Thesis

Chapter 2 describes basics of PET/CT physics and instrumentation to understand the performance of the scanners. Chapter 3 describes the performance of the PET/CT scanner we tested including counting-rate characteristics and uniformity of response. Chapter 4 discusses the effect of contrast agents on attenuation-correction accuracy. Chapter 5 describes an investigation of partial volume effects and possible methods to recover activity concentrations. The final chapter provides a summary of the work and a brief discussion of potential future research directions.

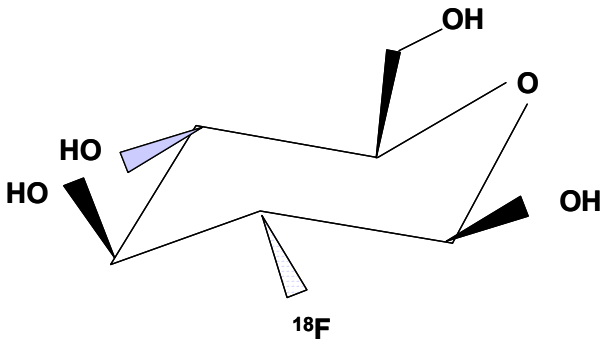

Figure 1-1: Structure of [^{18}F]-fluoro-2-deoxy-D-glucose

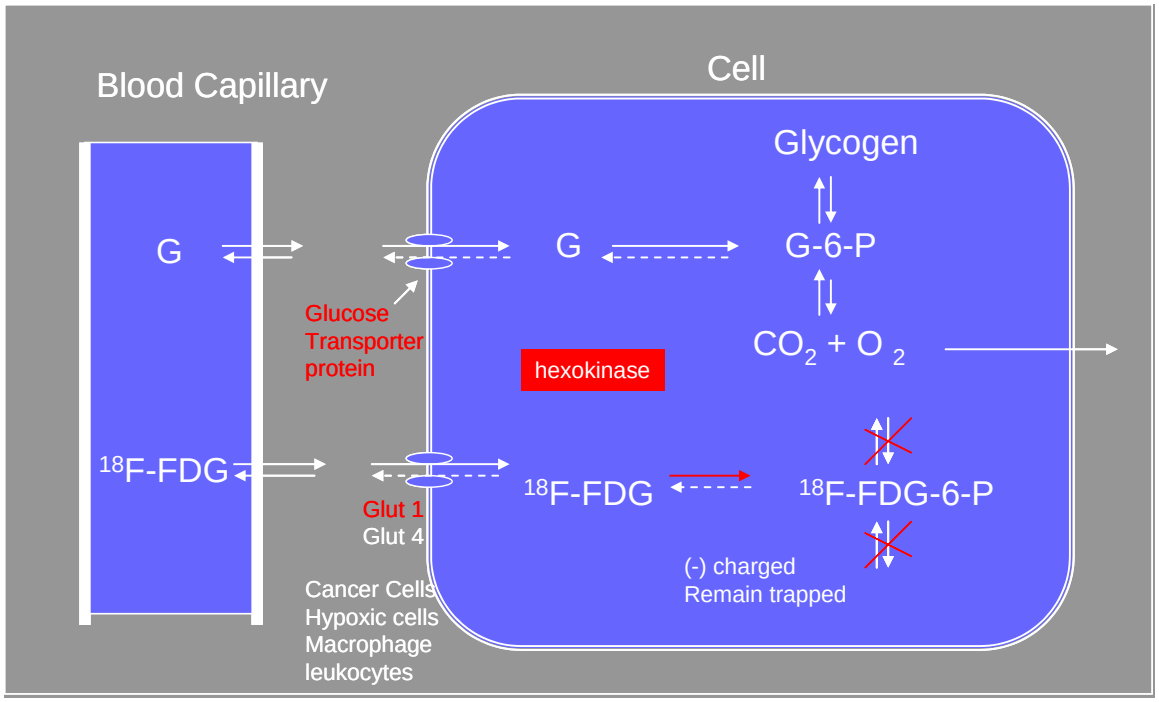

Figure 1-2: ^{18}F-FDG metabolism and intracellular accumulation. Adopted from Thrall JH. et al. Clinical Molecular Imaging. ACR-ASTRO 2003 Molecular Imaging Conference

Chapter 2

Related Physics

2.1 Instrumentation and Physics of PET/CT Scanner

2.1.1 Positron Decay

Many proton rich radionuclides decay via positron emission into a more stable state. A proton is converted into a neutron, a neutrino, and a positron.

$$ {}_1p^+ \rightarrow {}_0n + {}_1\beta^+ + \nu \qquad (2) $$

$$ {}_ZX \rightarrow {}_{Z-1}Y + {}_1\beta^+ + \nu $$

A positron is the anti-matter of an electron. The positron emitted from the nucleus will lose kinetic energy by interactions with the surrounding matter. The path is deflected from its original path by any of four types of interactions: inelastic collisions with atomic

electrons, elastic scattering with atomic electrons, inelastic scattering with a nucleus, or elastic scattering with a nucleus. The positron takes a torturous passage through matter, which complicates the estimation of range. Eventually, the positron and an electron may form a metastable intermediate species, positronium. The electron and positron revolve around their center of mass; positronium's half-life is about 10^{-7} seconds. The positronium formation occurs in about one-third of cases in water or human tissue while direct annihilation occurs the rest of the time [23].

When the positron and electron annihilate, they give off electromagnetic radiation. The most probable mode is rest mass converted into two photons of 511 keV each, propagating at 180 degrees to conserve momentum when the positronium has no residual kinetic energy (Figure 2-1). This principle is used to determine the line of response in the PET scanner. At less than 1% probability, three photons can be emitted. Also, not all annihilation events are zero-momentum; to safisfy momentum-conservation, these photon pairs are not exactly emitted at 180 degrees (a maximum deviation of ±0.25 degrees) [24]. In water, about 65% of annihilations deviate from co-linearity. This effect contributes resolution blurring of 1.5 mm to 2.0 mm for 80 cm to 90 cm diameter PET rings [23, 24].

There are several nuclides used in PET: ^{11}C ($T_{1/2}$: 20.3 min, max range in water: 5.4 mm) ^{13}N (9.97 min, 5.4 mm)), ^{15}O (124 sec, 8.2 mm), and ^{18}F (110 min, 2.4 mm). ^{18}F-FDG is the predominantly used radionuclide for PET imaging because of its relatively long half life.

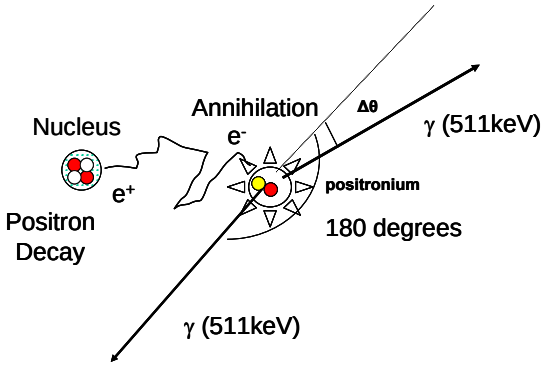

Figure 2-1: Illustration of positron decay and annihilation photons. The positron takes a torturous passage through matter and interacts with an electron. A metastable species, positronium, is formed about one-third of the time in water. Upon annihilation, the rest mass is usually converted into two photons of 511 keV at 180 ± 0.25 degrees.

2.1.2 Photon Interaction in Matter

Among photon interactions -- coherent scattering, photoelectric effect, Compton scattering, and pair production -- photoelectric effect and Compton scattering are particularly important in PET imaging physics. For soft-tissue and bone, the total attenuation coefficients are dominated by photoelectric absorption in the photon energy range below 100 keV and dominated by Compton scattering in the photon range of 200-1000 keV [25].

- **Photoelectric effect**

Photoelectric effect dominates in human tissue at energies less than 100 keV. The fact is important for PET/CT scans that use CT data for attenuation correction. Mean CT photon energy is at 70 keV. The mass attenuation coefficient for photoelectric absorption is approximately:

$$\frac{\mu}{\rho} \propto \frac{Z^{4.5}}{E^3} \qquad (3)$$

for photon energies from 10 keV to 500 keV and atomic numbers from 1 to 92.

- **Compton Scattering**

Compton scattering is directly proportional to Z and inversely dependent on photon energy from 10 – 1000 keV. Monte Carlo simulation of the interaction of annihilation photons with tissue-equivalent material in PET shows that more than 80 percent of scattered events that are detected have undergone only a single scattering interaction [23].

2.1.3 Photon Spectrum

PET images are based on detecting monoenergetic photons (511 keV) produced by annihilations. X-ray tubes produce a continuous bremsstrahlung spectrum which also contains characteristic X-rays with discrete energies corresponding to the transitions of orbital electrons in the high-Z target material, typically tungsten (Figure 2-2).

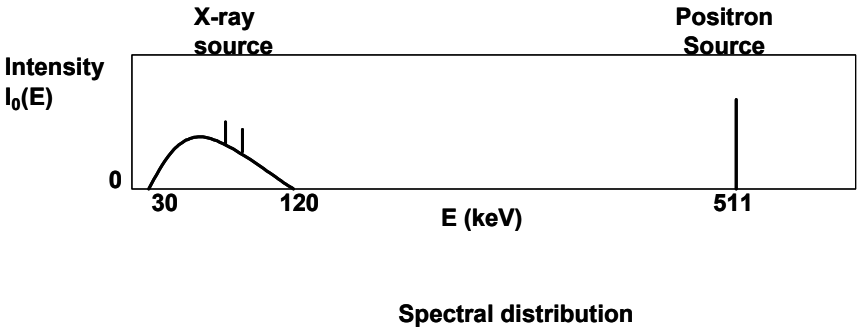

Figure 2-2: Photon energy spectral distribution for x-ray source and positron source [25].

Low energy photons are absorbed in matter by photoelectric absorption, shifting the average spectral energy to the right. This beam hardening effect causes significantly

undesirable effects on X-ray imaging because it introduces image contrast variations depending on the photon paths in addition to the object attenuation properties.

An X-ray CT detector operates in charge-integration mode and does not have energy discrimination, unlike a nuclear medicine detector. PET detectors operate in single-photon counting mode and have energy discrimination, ideally allowing rejection of scattered photon counts.

2.1.4 True, Random and Scattered Events

- **True and Random Events**

To be considered a valid event, the PET scanner must detect two 511 keV events simultaneously in two different detectors (Figure 2-3). The system assigns a line of response (LOR) for coincidence events, a straight line connecting the two detectors. Ideally, the positron annihilated somewhere along this LOR.

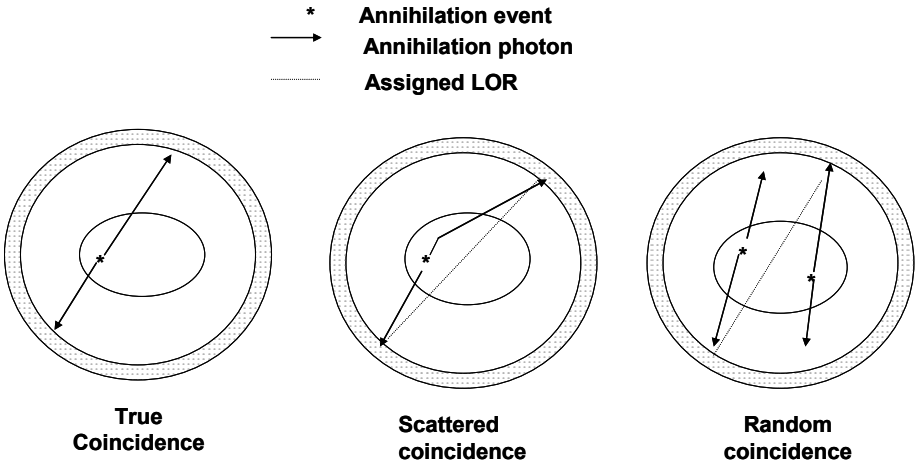

Figure 2-3: True, scattered, and random events

The difference in time window (Figure 2-4) is set under consideration of the following factors: time of travel of two annihilation photons, the detector's scintillation time, and the electronics' processing time. The scintillation time affects the time resolution, which is the uncertainty in the timing characteristics due to fluctuation of scintillation decay. A detector with short scintillation time constant has a small timing resolution. The maximum difference for time of travel by each photon before interaction in the detectors is about 3.33 ns using speed of light ($3x10^8$ m/s) and for a 1 meter scanner diameter. At time T, if detector 1 produces a signal, then any signal produced by detector 2 between $T+\tau_c$ and $T-\tau_c$ is considered a coincident event. The resolving time of the circuit is the coincidence time window and expressed as $2\ \tau_c$.

Random events occur when photons from different annihilations reach the detector within the coincidence time window. If S_1 and S_2 are singles count rates on channel 1 and 2 (counts/second), the random (R) events can be expressed as follows.

$$R_{12} = 2 \cdot \tau_c \cdot S_1 \cdot S_2 \qquad (4)$$

For example, for a typical bismuth germanate $Bi_4Ge_3O_{12}$(BGO) scanner, the coincidence time window is set to 12.5 nsec.

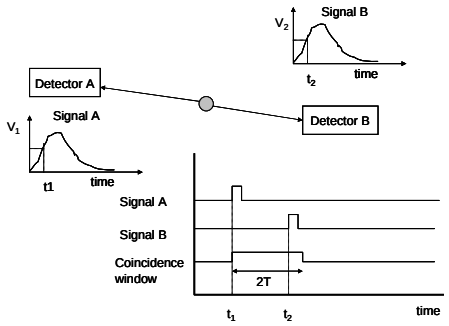

Valk PE et. al. Positron Emission Tomography. Springer 2002

Figure 2-4: Illustration of the coincidence true window. Signal B is in coincidence with signal A if it occurs any time within the coincidence time window.

From this equation, the total random rate is approximately proportional to the square of total count rate for all detector pairs. To minimize random coincidences, one can decrease the coincidence window; however this introduces statistical error due to event triggering fluctuation. The use of fast scintillators [decay constant - GSO: 60 nsec, lutetium oxyorthosilicate doped with cerium Lu_2SiO_5 (LSO): 40 nsec] can reduce the time window. However, it can not be reduced more than the time-of-flight (3-4 nsec) that is set by the scanner diameter. The optimal window is typically set to 3-4 times the full width at half maximum (FWHM) timing resolution of the PET scanner. The typical coincidence time window is 12 ns for BGO-based systems and 8 ns for GSO and NaI(Tl)-based systems.

All coincidence events are called prompt events and are expressed as

Prompts (P) = trues (T) + scatters (S) + randoms (R)

$$T = P - S - R \qquad (5)$$

By using this formula (4) and (5) with known S_1 and S_2, random events can be removed statistically from prompts. However, randoms correction process results in propagation of noise in the data set; therefore the best solution is to reduce random events either by reducing the count rate or by using a smaller coincidence time window. This is the reason why a PET scanner with good timing resolution is desirable.

- ## Scattered Events and Energy Windows

A certain portion of photons created in the body will interact in the body either by photoelectric absorption or Compton scattering. A Compton-scattered photon propagates in a different direction than the original unscattered photon. Coincidence events due to scattered photons cause misinterpreting of LORs and misrepresenting the true activity

distribution within the image (Figure 2-3). This causes blurring in the image, therefore it is important to remove these events.

Scatter is an especially important component of the signal in 3D imaging compared to 2D imaging where scatter contributes only a minor part of the signal [26]. In 3D imaging the calculated activity count rate is modified as follows:

$$A \propto \left[P - \left(\frac{S^{scattered}}{\eta^{scatter}} \right) - R \right] \times AC \times DT \times \eta^{true} \qquad (6)$$

AC: attenuation correction factor (See Chapter 3)

DT: dead time correction

η^{true}: normalization coefficient for scattered coincidence

$\eta^{scatter}$: normalization coefficient for true coincidence

$S^{scattered}$: scattered count rate

There are several efforts to approximate these normalization coefficients. Unfortunately, the scatter normalization coefficient is not a unique value (it depends on scattering angle). However, variation in scatter normalization coefficients is probably negligible compared to the scatter estimate itself.

Ideally, we should set the energy window exactly at 511 keV to reject all scattering events. This cannot be done for real PET scanners: scintillation crystals have a limited energy resolution; setting the energy window too wide will accept too much scatter, degrading image quality. If we set the energy window too narrow, it will reject some true events. Commercial PET scanners use wide energy windows to achieve high sensitivity, at the expense of accepting some scattered events. NaI(Tl) based scanners have good energy resolution (10–15%) and the energy window is set from 435 keV to

590-665 keV. BGO crystals have worse energy resolution compared to NaI(Tl) crystals. A typical BGO scanner's energy window is set from 300-350 keV to 650 keV. [24].

One of the methods to reduce scattering events is use of lead or tungsten septa (i.e. 2D mode). In multi-ring scanners, septa reduce scattered photons reaching the detectors. Septa also reduce the sensitivity of the scanner. Another method is to mathematically correct scattering events by using object-scatter models; however, scatter is very object-dependent. Currently, simple but computationally efficient models are used, but these are inherently limited in their accuracy. Monte Carlo methods can provide more realistic models but are too computationally intensive for clinical practice; recent developments of acceleration techniques eventually may make Monte Carlo methods feasible for clinical practice [27].

2.1.5 Sensitivity and Depth of Interaction

The sensitivity of a PET scanner is determined by its geometry and detector stopping power. The ideal geometry of PET scanners is (1) a small diameter and large axial field of view (FOV), and (2) a scintillation detector with high stopping power and high energy resolution. After a photon enters the detector, it travels a short distance before depositing its energy. Typically, the event registers the LOR as a connection of two points on the entrance surfaces of the detectors rather than the two actual interaction points. The error from this assumption becomes large when the photons enter at an oblique angle and with thick detectors. This parallax error is worst when annihilation occurs in the periphery of the scanner's FOV. The thickness of the detector trades off sensitivity and stopping power with parallax error. Detectors providing depth-of-interaction measurement are under research, e.g. [28].

2.2 Photon Attenuation and Attenuation Correction Factors

2.2.1 Attenuation Correction Factors

Suppose the scanned body consists of a homogeneous material, and d_1 and d_2 are the distance each annihilation photon traveled through the tissue (Figure 2-5). Then the probability of uncollided photons emitted along line D escaping from an object is given by

$$P = \exp(-\mu \cdot d_1) \cdot \exp(-\mu \cdot d_2) = \exp(-\mu \cdot (d_1 + d_2) = \exp(-\mu \cdot D) \qquad (7)$$

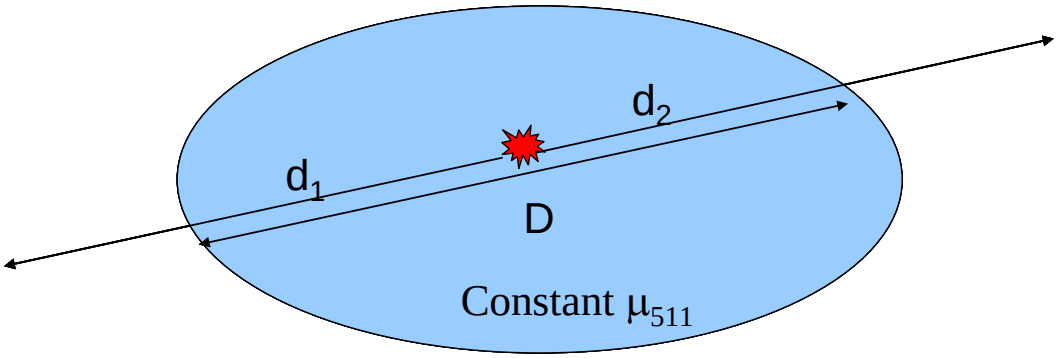

$$ACF = \exp(+\mu \cdot d_1 + \mu \cdot d_2) = \exp(+\mu \cdot D)$$

$$\textit{Uncollided photons emitted from the object along line } D = N_0 \cdot \exp(-\mu \cdot D)$$

$$\textit{Uncollided photons emitted from the object along line } D \times ACF = N_0 \cdot \exp(-\mu \cdot D) \cdot \exp(+\mu \cdot D) = N_0$$

Figure 2-5: Attenuation correction factor in homogeneous material

If the attenuation coefficients along the LOR are not uniform (Figure 2-6), then the relation becomes

$$P = \exp\left(-\sum_{i=o}^{x} \mu_{1i} \cdot d_{1i}\right) \cdot \exp\left(-\sum_{i=x}^{l} \mu_{2i} \cdot d_{2i}\right) = \exp\left(-\sum_{i=0}^{l} \mu_i \cdot d_i\right) \quad (8)$$

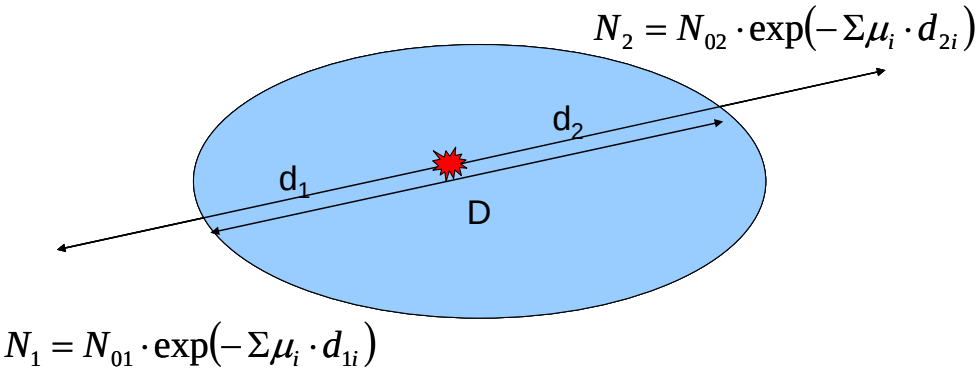

Figure 2-6: Attenuation correction factor in heterogeneous material.

We know that for each LOR the ratio of I_0 (blank scan) to I (acquired transmission scan) is

$$\frac{I_0}{I} = \exp\left(\sum_{i=0}^{l} \mu \cdot d_i\right) \quad (9)$$

The factors to correct non-uniform attenuation correction coefficients are called attenuation correction factors (ACFs) and they are obtained from transmission scans. Widely-used attenuation correction factors are obtained using (1) positron sources, (2) gamma-ray sources, and (3) x-ray sources (Table 2-1). If we use an emission source other than a positron emitter, we must re-scale the attenuation correction factors since the attenuation coefficients are energy dependent. There are three methods for emission scans: (1) positron sources: ^{68}Ge/ ^{68}Ga [β+ emitter (511 keV annihilation photon),

transmission data from coincidence events]; (2) γ-ray Sources: ^{137}Cs [a γ emitter (662 keV) and single events are collected as a transmission scan. The attenuation correction factors obtained are at 662 keV, not at 511 keV, and require scaling down. Both scaling and segmentation methods were used for this correction]; (3) CT sources, which describe next.

- **CT Sources**

There are four advantages of using CT scan for transmission scans: (1) lower statistical noise compared to the radionuclide sources, (2) faster acquisitions, (3) no contamination from emission photons, (4) it does not require periodic replacement of positron sources, and (5) CT with PET can be used to localize activity in relation to anatomy. The disadvantage of using CT scan for ACFs is that it requires re-calculation of ACFs at 511 keV from attenuation coefficients obtained from 30-140 keV spectrums by CT scans. There are three conversion methods: segmentation, scaling, and dual-energy CT scans.

Table 2-1: Comparison of the transmission methods for PET [25].

Sources	positron	single gamma	X-ray
Photon energy (keV)	511	662 for Cs-137	continuous:~30 to 140
Patient scan time (min)	15 - 30	~ 5 - 10	~ 1
Transmission noise	highest	high	insignificant
Potential for bias/artifacts	low	some	highest

- **Segmentation**

Segmentation classifies CT images into different tissue types (such as soft tissue, lung, and bone). Then CT values are changed to corresponding attenuation coefficients at 511 keV. A problem arises when the tissue changes value continuously (in the lungs,

up to 30%); replacing by a single attenuation coefficient at 511 keV potentially introduces an error [25].

- **Scaling**

The images created by CT are approximately linearly correlated to the attenuation coefficients of soft tissue. CT values multiplied by the ratio of the attenuation coefficients at 511 keV and at mean CT energy are called scaling [1, 25]. For low-Z material, the approximation of the attenuation coefficient is accurate when multiplied by scaling factors. However, different scaling factors are necessary for bones, because linear scaling is a poor approximation. This is because the high Z value of calcium (Z=20) leads to higher photoelectric attenuation coefficients at CT energies.

Another method, called the "hybrid method" is a combination of scaling and segmentation (Figure 2-7). This separates bone and non-bone components and then uses separate scaling factors for each component. There is a discontinuity at 300 HU. The "bilinear method" is piece-wise continuous [25]. Although both the hybrid and bilinear methods give reasonable approximations for biological materials, in the presence of contrast materials and metal objects, the approximations are still inaccurate.

- **Dual Energy X-ray Imaging**

By scanning two or more spectra of an x-ray beam, CT numbers can be converted into 511 keV linear attenuation coefficients as a weighted sum of photoelectric absorption and Compton scattering. The problem of this method is errors caused by image noise.

CT scan is not the only-method to map attenuation coefficients throughout the body. For instance, T1-weighted magnetic resonance imaging (MRI) has been investigated for attenuation and scatter correction in 3D brain PET imaging [29].

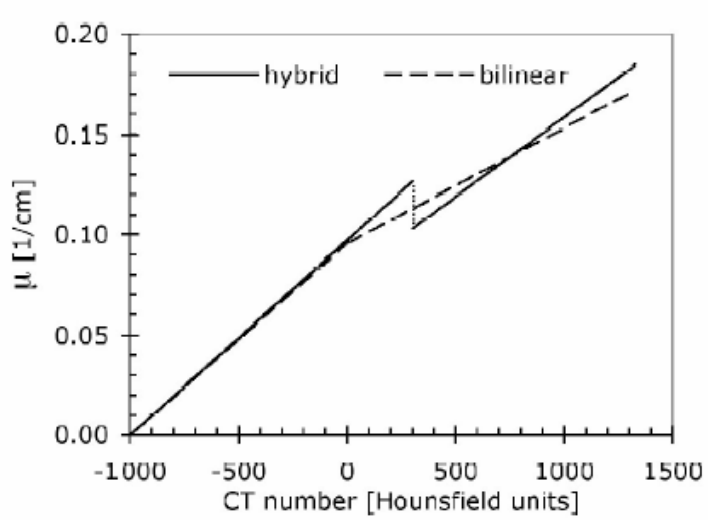

Figure 2-7: Conversion of CT numbers to linear attenuation coefficients at 511 keV. The hybrid method has a discontinuity at 300 HU and the bilinear method has a change in slope at 0 HU [25].

2.2.2 Problems for CT-based Attenuation Correction

A mismatch of calculated and true attenuation coefficients introduces biases and artifacts in the reconstructed PET images.

- **Spatial Mismatch**

CT scans are usually obtained at end-inspiratory phase as opposed to PET scans, which are obtained as respiratory-averaged images. This causes spatial mismatches. One of the solutions is to acquire CT images during the partial expiratory phase to match with the PET emission images under the sacrifice of diagnostic quality of CT images. Respiratory gating and motion tracking devices are under investigations [21, 22].

- **Truncation Artifacts**

PET scanners often have larger FOV (50-70 cm) than a CT scanner's FOV (45-60 cm). PET scans are often obtained with the patient's arms next to the body while the

arms may be raised during the CT scan. For a large patient, some part of the body may be outside the CT's FOV, resulting in some bias of the reconstructed activity distribution due to erroneous ACFs [13].

- **Metal Implant**

Many oncological patients have metal implants such as chemotherapy ports, pacemakers, dental fillings, and artificial joints. These high-Z materials cause significant artifacts in the attenuation correction factor obtained in the CT energy range. It is especially important to reconstruct attenuation uncorrected images in these patients.

- **Contrast Agents**

Intravenous (IV) contrast agents are composed of iodine (Z=53) at concentrations of 300-380 mg/mL. Typically, 100-200 mL of IV contrast agent is injected as a bolus at a rate of 1.5 to 5 mL/s [25]. The distribution of contrast agent depends on the time after injection. Over time, the agent is excreted through the kidneys, ureters, and bladder. Oral contrast agents are either barium (Z = 56) based or iodine based. Because of increased attenuation due to high Z, these contrast agents produce contrast in a CT image.

Immediately after a bolus injection, the CT numbers of highly vascularized tissue increase to 200-300 from 30-60. At 511 keV the mass attenuation coefficient of iodine is about the same as water or soft tissue (Figure 2.8). Therefore, any scale factor that correctly predicts the attenuation factor at 511 keV for bone or soft tissue will overestimate the attenuation at 511 keV for contrast agents [25]. According to recent literature, intravenous contrast at normal concentrations has little effect on the CT-based ACFs, but for oral contrast, larger intestinal volumes and a wide range of concentration (about 170 HU in the stomach, about 700 HU in lower gastrointestinal tract where water

is absorbed) can potentially cause overestimation of ACFs [1]. A recently-proposed approach to avoid over-estimation of ACFs is, for pelvic gastrointestinal oral contrast agent, the use of negative oral contrast agent [13].

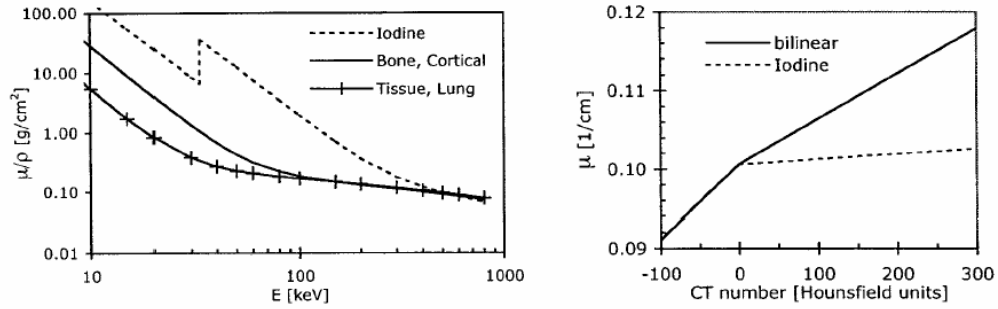

(a) Mass attenuation coefficient vs. energy

(b) Linear attenuation coefficient vs. CT #

Figure 2-8: Comparison of scaling of attenuation coefficients. (a) The mass attenuation coefficient is significantly enhanced at CT photon energies for iodine, but at 511 keV it is similar to other materials. (b) Comparison of the linear attenuation coefficient at 511 keV vs. CT numbers predicted with the true value for iodine. [25]

2.3 Image Reconstruction Algorithms

2.3.1 Overview of Reconstruction Algorithm

PET data is acquired in either 2D or 3D mode. The 3D mode requires more memory and more computational time. Filtered-backprojection algorithm (FBP) is a classical analytical reconstruction algorithm widely used for computed tomography. In contrast to analytical algorithms, iterative algorithms assume a statistical distribution of the data is derived from a Poisson model. Recent developments of fast iterative algorithms allow more accurate reconstruction of acquired data. The ordered subset expectation maximization (OSEM) algorithm in 2D mode is widely used in commercial

PET/CT scanners. 3D iterative reconstruction is independent of geometry, but it is computationally intensive. Hybrid algorithms combine efficient 2D iterative algorithms with a fast rebinning algorithm, where 3D data is reduced into 2D data.

2.3.2 2D Data

- **Analytic 2D Reconstruction**

The Radon transform of an object $f(x,y)$, denoted as $g(s,\phi)$, is defined as its line integral along a line inclined at an angle ϕ from the y-axis and at distance *s* from the origin.

Mathematically, it is written as

$$g(s,\phi) \equiv \Re f(x,y) = \int_{-\infty}^{\infty}\int_{-\infty}^{\infty} f(x,y)\delta(x\cos\phi + y\sin\phi - s)dxdy \quad (10)$$

where $\Re$ is the Radon transform operator.

In medical imaging, we are interested in recovering $f(x,y)$ from the sinogram $g(s,\phi)$, which is the measured PET data, after corrections for scatter, randoms, and attenuation.

Associated with the Radon transform the back-projection operator is defined as

$$b(x,y) \equiv \mathrm{B}g(s,\theta) = \int_0^{\pi} g(x\cos\phi + y\sin\phi,\phi)d\phi \quad (11)$$

The reconstructed image

$$\tilde{f}(x,y) \equiv Bg = B\Re f \quad (12)$$

is $f(x,y)$ blurred by the PSF $\dfrac{1}{(x^2+y^2)^{\frac{1}{2}}}$.

During reconstruction, filtering or deconvolution is used to remove the PSF blurring, recovering the original object *f(x, y)*. Details of the FBP reconstruction methods can be found in imaging textbooks [30, 31].

- ## Iterative Reconstruction

Filtered backprojection is computationally efficient. It is based on the assumption that the projection images are perfect projections of a three dimensional object. This is not true: Compton scattering, and photon attenuation factors in the patient affect the LORs. Iterative reconstruction has been developed to overcome this problem. An initial activity distribution in the patient is assumed, and then projection images are calculated from the assumed activity distribution. The calculated projection images are compared with the actual images and the assumed activity distribution is modified and recalculated [32].

The most widely used iterative algorithms in PET are the maximum-likelihood expectation maximization (ML-EM) algorithm and its accelerated version OSEM. OSEM was proposed in 1994 and is sufficiently fast for clinical applications. With each iteration, the target function is updated several times, proportionally accelerating convergence. An optimization of subsets and iterations is required when the method is applied to real noisy data. The detail of the algorithm is explained elsewhere [23, 24].

- ## 3D Analytical Reconstruction by Rebinning

Reconstruction of 3D PET data requires large amounts of memory due to the large number of LORs. Strictly, 2D mode produces N sinograms. In practice, in a multi-ring system, we allow cross-slices and having 2N-1 detector rings. A full 3D mode produces N direct transaxial slices and N (N-1) oblique sinograms (N^2 in total).

Rebinning is a method to estimate 2D transaxial sinograms from oblique sinograms acquired in 3D mode. Two rebinning approaches are commonly used: single-slice rebinning (SSRB) and Fourier rebinning (FORE) [23]. SSRB assumes that each measured oblique LOR only traverses a single transaxial section within the support of the tracer distribution and average overall available estimates. SSRB induces axial blurring and transaxial distortions because of its approximations. FORE is more accurate than SSRB. Fourier transforms and normalization are used to rebin the data according to septal frequency information After inverse 2D Fourier transform, the rebinned transaxial slices are obtained. This algorithm assumes that the data are line integrals of the tracer distribution and each oblique sinogram is sampled fully. FORE is sufficiently accurate in practice when the axial aperture is less than 20 degrees [23].

Chapter 3

Uniformity of Activity Concentration of Discontinuous Positron Emitting Sources

3.1 Instrumentation of PET/CT Scanners

3.1.1 True, Scatter, and Random Events and Energy Window

In a clinical PET/CT exam, approximately 10 mCi ^{18}F-FDG is injected intravenously into the patient. It is important to understand how the physical performance of the PET/CT scanners produces the observed image quality. To assess the performance of the CTI-Siemens PET scanner, we recorded true, scattered, and random coincidence events for different activity levels. Energy windows are set by the

manufacturer and we do not have equipment to test the energy window width directly in our facility.

3.1.2 Materials and Methods

Data in this study was acquired with a CTI-Siemens Reveal-HD (Knoxville, TN). The acquisition and reconstruction protocols use the following manufacturer's settings (Table 3-1).

Table 3-1: Acquisition and reconstruction parameters of CTI-Siemens Reveal-HD.

F-18 half-life (sec)	6586.2
Sinogram dimensions	3
matrix size [1]	228
matrix size [2]	228
matrix size [3]	239
Scale factor (mm/pixel) [1]	2.25
Scale factor (mm/pixel) [2]	1
Scale factor (mm/pixel) [3]	2.425
Holizontal bed translation	stepped
Axial compression	9
Maximum ring difference	22
Number of segment	5
Total number of sinogram	239
Lower energy window (keV)	350
Upper energy window (keV)	650
Number of rings	32
Axial FOV (cm)	15
TransverseFOV (cm)	66
Scintilation Cristals	BGO
Number of PMTs	576
Total number of block bucket	96
Number of image planes	47

A ^{18}F-FDG source was drawn into 5mL syringes and the activity was measured with a well counter (CRC-15R, Capintec, Inc., Ramsey, NJ). Each syringe was placed at the center of a cylindrical acrylic phantom with 20 cm diameter. The center of the phantom was aligned to the center of the FOV using the PET/CT scanner's laser indicator. For

each source, true, scatter, and random events were recorded. Emission data were scanned using default settings for a thoracic scan (Thorax C-A-P + C) with one PET bed and a 5-minute acquisition time. Images were reconstructed with OSEM4i8s (4 iterations 8 subsets) with 128x128 matrix and FORE 3D sinogram rebinning. ACFs were obtained from helical CT scan data with parameters of 120 kVp, 80 mA, 0.8 s per CT rotation, 3 s delay, 83 sec scan time.

3.1.3 Results and Discussions

For ^{18}F-FDG, our scanner demonstrated a linear relation between activity concentration and singles counts for activity less than 10 mCi (Figure 3-1). True counts (coincidence events) were saturated approximately at 2 mCi with 1.7 x 10^6 counts/second (cps).

In the clinical patient setting, the recommended dose for a 70 kg adult patient is 5-10 mCi. The typical dose given to an adult patient for a whole body PET scan is 10 mCi. A patient fasts for 4-6 hours prior to the injection. After injection, the patient rests for 45-60 minutes; before the PET/CT scan, the patient is asked to void the bladder. The amount of ^{18}F-FDG in the bladder depends on many factors including the patient's renal function. In the literature it is documented that approximately 20% of ^{18}F-FDG is discovered in the urine at 2 hours after the injection [33]. FDG's half life is 110 minutes. A rough estimation without considering attenuation and distribution of the tracer in the body is

$$A(60\,\text{min}) = A_0 \bullet \exp\left(-\ln 2 \bullet \left(\frac{60}{110} \right) \right) \qquad (13)$$

If A_0 = 10 mCi, then after A(60 min) = 6.85 mCi.

Approximately 20% of ^{18}F-FDG appears in the bladder. The remaining activity in the body is about 6 mCi at the time of scanning. Typical whole body PET uses 6 bed positions. Ignoring the lower body, the rest of the body is about 4 PET beds. Then neglecting the scattering from outside of FOV, approximately 1.5 mCi of activity is located in one PET bed. Comparing to Figure 3-1, a 10 mCi dose is likely to be under saturation of the PET scanner's true counts.

As described in the instrumentation section, BGO crystals have good stopping power, but poorer light yield and resolution than NaI(Tl) crystals. BGO crystal's energy resolution is 25%; LLD is set to 350 keV; and ULD is set to 650 keV. A 3D PET scanner does not have septa between the BGO crystals. A 3D mode acquisition improves statistics by increasing the number of counts, but at the expense of increased scattered and random events.

Accepting more counts has an advantage for patients by reducing tracer activity and reducing acquisition time. However, 3D mode image reconstruction is computationally intensive. Furthermore, the 3D mode suffers from blurring of images by accepting more scattering events as true counts. This problem is not only from inside of FOV but also from outside of the FOV. This may cause problems in image quality: organs located outside of FOV with high ^{18}F-FDG concentration such as brain or bladder possibly contribute scattered events into the FOV.

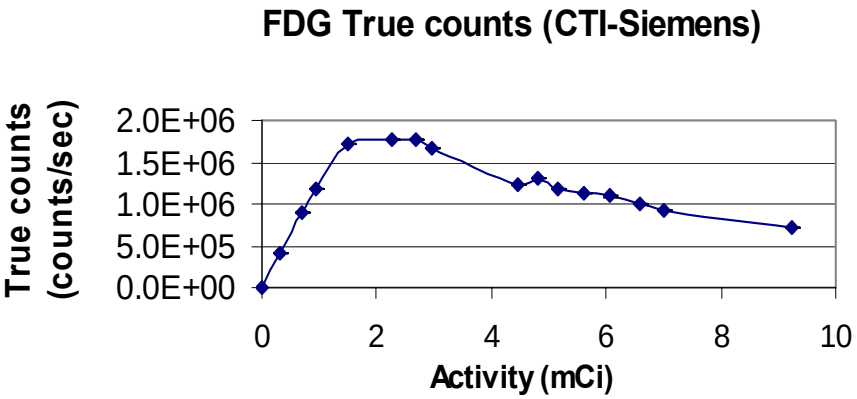

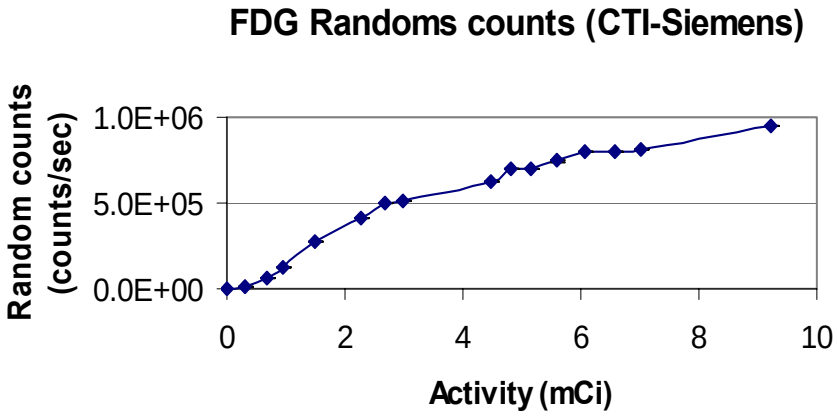

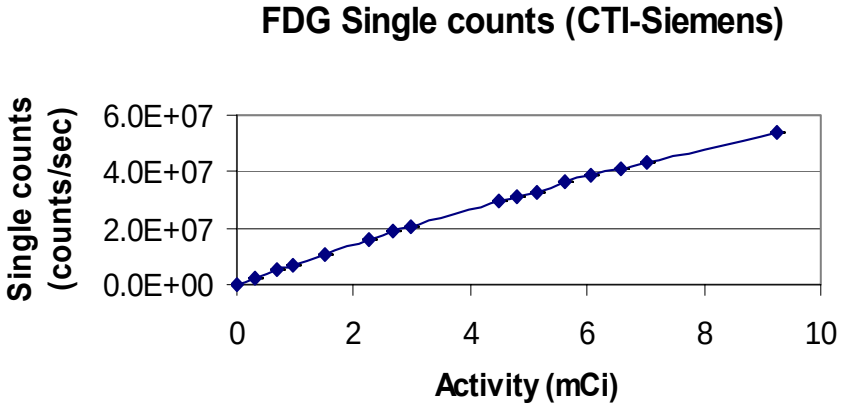

Figure 3-1: Relation between the activity (in 5mL syringe) at the center of the field of view and the measured true, random, and single counts. The source was ^{18}F-FDG.

3.2 Uniformity of the Radioactivity Concentration

3.2.1 Normalization and Uniform Activity Concentration source

In PET instrumentation the best resolution is achieved at the center of the FOV. In the ideal system, resolution and sensitivity are constant through out the FOV. It is well known that lines of response (LOR) in a real PET scanner have different sensitivity for many reasons, such as solid angle subtended (Figure 3-2), intrinsic variation in detector efficiency (e.g., variation in detector gain), detector penetration, septal absorption, detector packing fraction , and event timing errors [23, 34]. Therefore, normalization coefficients are applied to each LOR to minimize these factors. The direct normalization method uses uniform activity cylindrical ^{68}Ge volume source to measure the normalization coefficients. Ideally, normalization removes sensitivity variations from the data before image reconstruction.

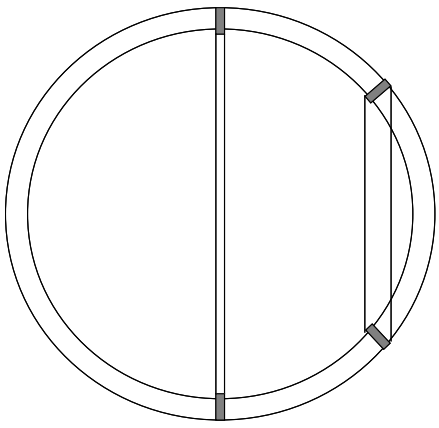

Figure 3-2: Illustration of solid angle effects.

The normalization method assumes that the normalization coefficients are applicable to discrete sources, such as one finds for lesions in the clinical setting. This is a critical assumption for accurate quantitative analysis. We scanned a 1 mL uniform source over the FOV as a pilot study. The source was composed of ^{18}F-FDG in a micro centrifuge tubes. The result was surprising: recovered activity concentration varied with location in the x-z plane (Figure 3-3). The recovered activity concentration varied by 36%. The next section describes an expanded experiment to further investigate this problem.

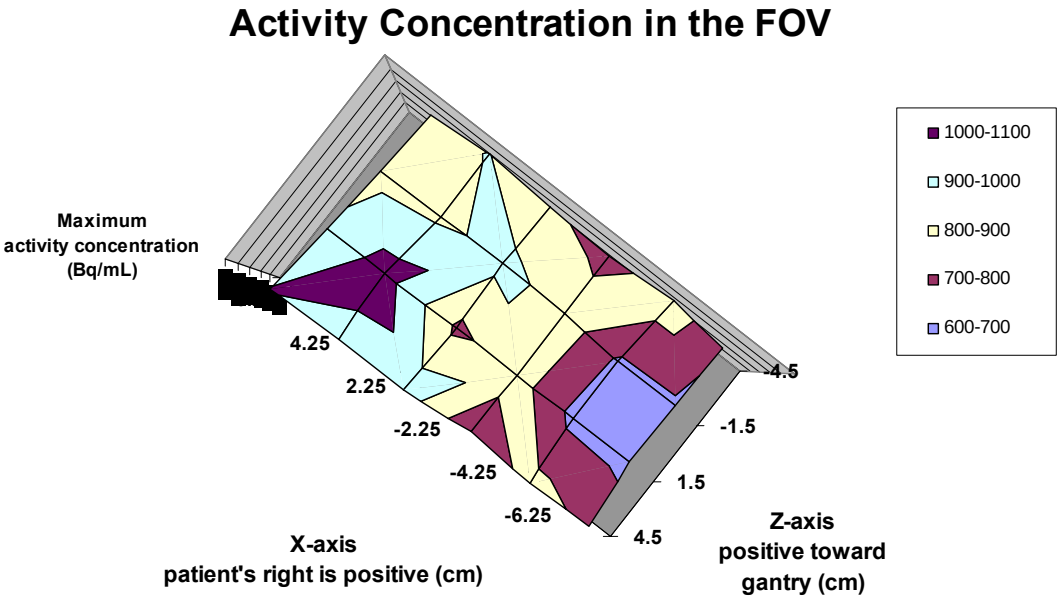

		X-axis (cm)					
		6.25	4.25	2.25	-2.25	-4.25	-6.25
Z-axis (cm)	4.5	1004	968	959	715	833	778
	1.5	924	1041	780	851	671	665
	-1.5	858	880	927	864	685	681
	-4.5	804	903	818	766	855	716

Figure 3-3: Variation of the measured activity concentrations as a function of location in the FOV. The micro-centrifuge tube was scanned over a 6 x 4 grid. The maximum activity concentration at each location was recorded. The table reports the activity concentrations and the surface plot displays the results graphically.

3.2.2 Materials and Method

Twenty-one micro-centrifuge tubes (inner diameter 9 mm; height 35 mm) were arranged in a Styrofoam disk (diameter 20 cm, thickness 2.5 cm) as shown in Figure 3-4. Each tube was arranged in a grid and separated by 4 cm. ^{18}F-FDG was prepared at the concentration of 0.2 µCi/mL in a 50 mL volume, mixed well, and each tube was filled completely with 1.7 mL of solution. The center of the disk was aligned to the center of the FOV; the disk was scanned in the following orientations: X-Y (transverse), Y-Z (sagittal), and Z-X (coronal) plane.

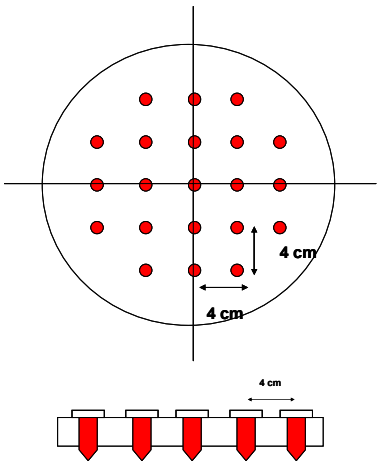

Figure 3-4: Arrangement of the micro-centrifuge tubes. Twenty-one micro-centrifuge tubes (inner diameter 9 mm; height: 35 mm) were placed in a Styrofoam disk (diameter 20 cm, thickness 2.5 cm). Each tube was arranged in a grid and separated by 4 cm. Each tube contained 1.7 mL of ^{18}F-FDG (0.2 µCi/mL).

The tubes were scanned using a clinical thoracic protocol (Thorax C-A-P + C). The helical CT attenuation correction scan used a 1 mm slice thickness, an effective current of 80 mA, and 130 kVp. Each PET scan was a 5 minute acquisition time with one bed position. The image reconstruction used the default OSEM 4i8s and FORE sinogram rebinning. Two reconstructed images with different matrix sizes (128 x 128

and 512 x 512) were derived from the same data set. The maximum activity concentrations of the objects were recorded from regions of interest drawn over all slices of each object. We used the maximum value (instead of average) as used in the PET/CT exam in the clinical setting.

3.2.3 Results and Discussion

Maximum activity concentration of each source in three planes is shown in Figure 3-5. For the X-Z and the Y-Z planes, the two outermost rows of tubes were not completely visualized because they were located outside of the 15 cm axial FOV. Consequently, maximum activity concentration values from these rows were not measured. The average maximum activity concentrations with standard deviations are given in Table 3-2. In Figure 3-5, the maximum activity concentration is plotted against the coordinates of the different planes and displayed as a continuous surface. Neither plane showed symmetry about the central X, Y, or Z axis (Figure 3-5). We wished to acquire a blank scan to see if this gradient of the activity concentration was induced by background radiation such as from the shielded cylindrical ^{68}Ge source in the examination room. However, we could not obtain a blank scan because of the clinical scanning software would not allow image acquisition with no activity in the FOV. If the room's background is substantial, background subtraction from acquired data should be used. In the future, one could scan a cylindrical ^{68}Ge source and examine the activity concentration profiles to see if this variation is introduced by the routine normalization processes. As in indirect check of room background, we surveyed the PET examination room with a survey meter (Biodex, Shirley, NY); the survey showed less than 100 cpm in

the PET's FOV. Thus, we expect that the background due to the ^{68}Ge source in the room is probably negligible.

Variations along the Z axis are less pronounced than along the X-axis and Y-axis (Figure 3-5 A and Figure 3-5 B). In all planes, the 512 x 512 matrix produced less variation than the 128 x 128 matrix reconstructions; however the pattern of variation did not seem to be preserved. Variation in the plane is reduced by the larger matrix size for the reconstruction algorithm. PET field of view is fixed. Increasing in matrix reduces the size of each pixel (128 x 128 matrix 5.15 mm; 512 x 512 matrix 1.29 mm). The sonogram matrix size is fixed by manufacturer. When the sonogram is converted into 128 x 128 matrix size in transaxial slices, it loses some information; the lower matrix grid is too large relative to the size of the object.

There is an optimal number of iterations to obtain the best image. Too many iterations can lead to noise amplification with deterioration in image quality [24]. We did not examine the effect of iteration number within the scope of this thesis.
One potential source of variation is the FORE rebinning process.

Table 3-2: Acquisition and reconstruction parameters of CTI-Siemens Reveal-HD.

	Matrix size	Average maximum activity concentration (Bq/mL)
X-Z plane	128 x 128	2766±438
	512 x 512	2356±31
Y-Z plane	128 x 128	2919±362
	512 x 512	2524±103
X-Y plane	128 x 128	3526±647
	512 x 512	2932±105

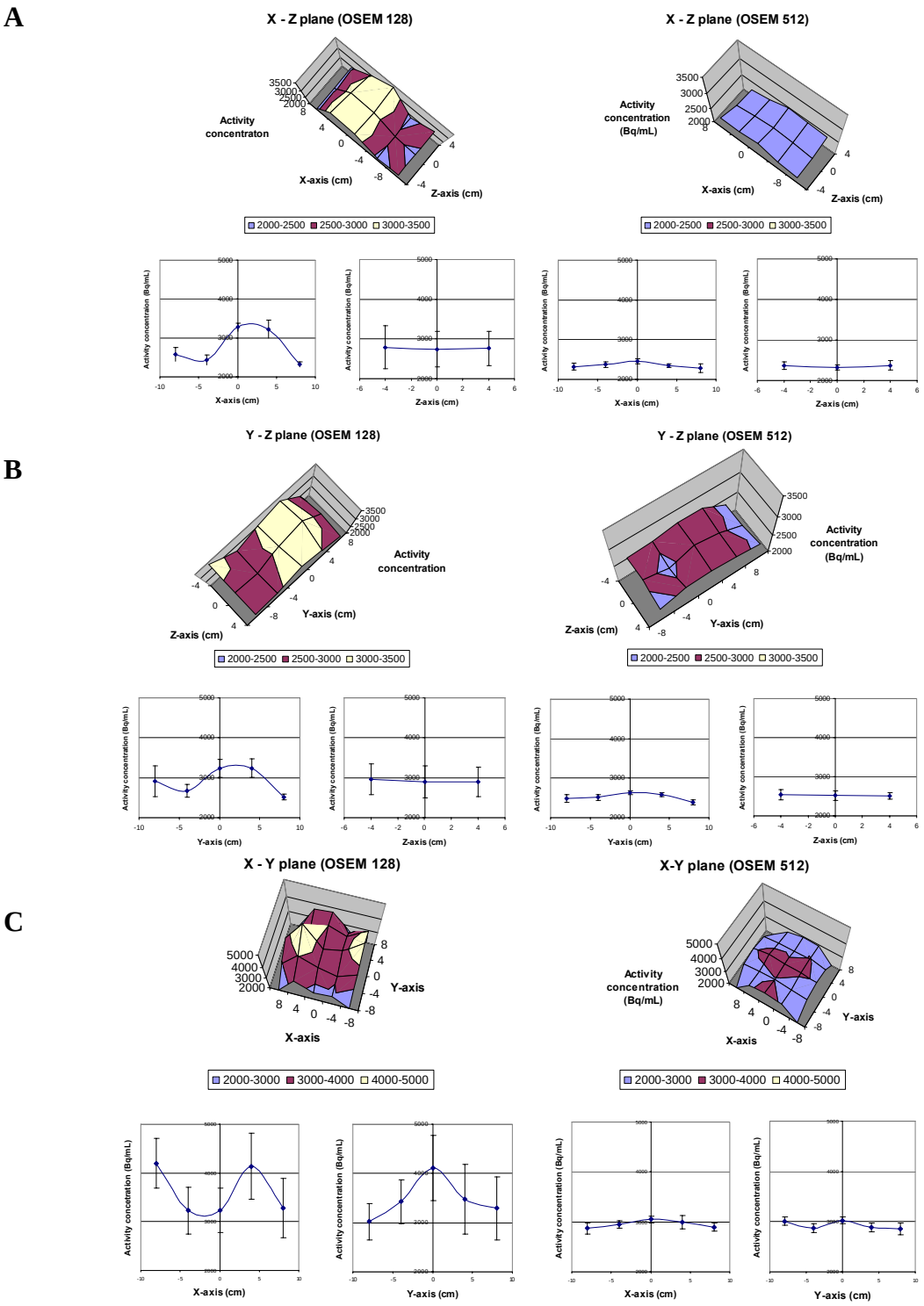

Figure 3-5: Maximum activity concentration in three independent planes (A: X-Z, B:Y-Z, C: X-Y). The maximum activity concentration of each object is plotted according to its coordinate in the planes. Both 128x128 and 512x512 matrixes were investigated. The curves in the 1-D plots represent the maximum concentration averaged in the orthogonal direction to the plot axis. Error bars represent standard deviation of the averaged values.

Sources placed in X-Y plane showed higher variation in activity concentration compared to ones in X-Z and Y-Z plane. The reason of this is probably attributed to the geometrical shape of the object. The X-Y plane produces the smallest transverse cross-section of the object among three planes because of the geometry of the micro-centrifuge tubes. The partial volume effect that is discussed in Chapter 5 induces more errors in activity concentration recovery in small objects. Imaging of spherical objects rather than cylindrical tubes might be one way to minimize this effect; however such objects were not available at the time of the experiments.

Although we demonstrated better activity concentration recovery with OSEM4i8s in 512 x 512 matrix, in the clinical setting, a 128 x 128 matrix size is widely used. For 128 x 128 matrix, it took 142 second to reconstruct images and for 512 x 512 matrix, it took 1251 sec. Our scanning was only for one PET bed. In a whole body PET scan for an adult patient, six PET bed positions are typical. If the smaller matrix size is the major factor inducing error in the uniformity across the FOV, then computation time would be a part of the reason why our clinical mode is set to the lowest matrix size. If the errors can be reduced by increasing matrix size, advancement of technology in minimizing computation time should allow us to use higher matrix size in reconstruction. We recommend using higher matrix size if we use PET data for quantitative purpose. Another consideration that we should note is that we acquired images in air. To simulate clinical situations, one should image the tubes in a cylindrical phantom filled with physiological background ^{18}F-FDG activity concentration. If we still see this non-uniformity for discrete sources under this setting, then calibrations for discrete source objects may be necessary, instead of or after the manufacturer's suggested normalization

process. However, the normalization processes are done daily by manufacturer-created routine QA software and we did not have access to data to understand what exactly this software is doing for normalization. To conclude whether another discrete source normalization process will improve accuracy of quantitation of the PET/CT scanner or not, extensive collaboration with the manufacturer is probably necessary.

Chapter 4

Contrast Agents and PET/CT Data

4.1 CT Numbers or Hounsfield Units (HU)

CT numbers are quantitative. CT numbers are used to identify the composition of a structure or lesion such as lung or bone. After CT reconstruction, CT number represents the relative attenuation coefficient of the tissue in that pixel, according to the formula [32]

$$CT(x,y) = 1000 \times \frac{(\mu(x,y) - \mu_{water})}{\mu_{water}} \qquad (14)$$

CT numbers are called “Hounsfield units” (HU). The CT images typically possess 12 bits of values ranging from -1000 to +3095

(air: -1000, soft tissue: between -300 and -100, water: 0, dense bone: +3,000).

4.2 Contrast Agents and Attenuation Correction Factors

4.2.1 Introduction

The benefits from the administration of contrast agents are significant especially in abdomen, pelvis, and head and neck studies. Oral contrast agents are widely administered in most CT imaging because they help radiologists distinguish the gastrointestinal tract mucosal surface from other tissue in CT images. Intra-venous (IV) contrast agents are also widely administered for CT for more accurate identification of vascular structures. Enhancement helps classification of lesions and also helps delineation of pathological lesions from normal structures such as muscles and vascular structures. Typical contrast agents are organic iodine (e.g., MD-Gastroview™ for oral contrast and Ominpaque™ for IV contrast) and barium sulfate (oral and barium enema). These agents are high atomic number materials; because of higher probability in photoelectric absorption, they enhance x-ray attenuation and hence contrast in image studies.

PET/CT studies are not an exception for use of contrast materials. PET/CT obtains ACF's from the CT scan. The method to obtain ACF's in PET image requires a step to convert attenuation coefficients at energies of 30 – 140 keV into 511 keV values (Figure 4-1). The algorithm used in the CTI-Siemens PET/CT has a threshold at 300 HU for converting either soft tissue or bone density. Therefore, high CT numbers caused by contrast materials are interpreted as bone and can be scaled into a wrong ACF at 511 keV.

Theoretically, these overcorrected values could possibly lead to false representations of the PET images [35, 36].

The majority of patients undergoing PET/CT are oncological patients and it is not infrequent for a patient to have a fluoroscopic study, receiving contrast agent for screening for gastro-intestinal (GI) malignancies, prior to the PET/CT scanning. Sometimes residual contrast agents in the GI tract are recognized after a topogram (patient-positioning) scan during PET/CT studies. Fluoroscopic contrast causes significant problems because a higher density of barium sulfate is used for these GI radiographs.

In PET, the standard uptake value (SUV) is widely used to quantitatively distinguish a malignant lesion from a benign lesion. The artifacts due to wrong HU scaling by contrast agents possibly may mislead physicians' interpretations of the PET/CT image. To investigate the effect of contrast material on SUV, first we tested HU for different dilutions of commonly used contrast materials. Second, we investigated its effects on recovered activity concentration.

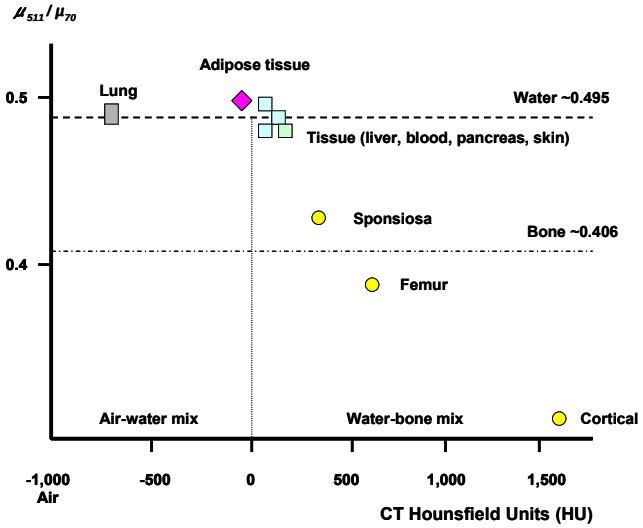

Figure 4-1: Plot of μ_{511}/μ_{70} as a function of HU. Scaling factors for soft tissue (water) and bone are indicated by horizontal lines [1].

4.2.2 Materials and Methods

Three types of commercial contrast agents were investigated. They are barium sulfate, oral iodine contrast, and IV iodine contrast.

Barium sulfate: Berry smoothie Readi-Cat 2™. Barium sulfate suspension 2.1% w/v (EZ-EM Inc. Westbuny, NY).

Oral iodine contrast: MD-Gastoview™. 367 mg/mL organically bound iodine. Diatrizoate Megalumine and diatrizoate sodium solution (Mallinkrodt Inc. St.Louis, MO)

IV iodine contrast: Ominpaque 300™ Injection. 647.1 mg/mL inhexol solution; 300 mg/mL organically bound iodine (Amersham Health Inc. Princeton, NJ)

- **Experiment 1**

The following contrast materials were prepared in a series of dilutions in water as follows: 0, 1, 2, 4, 10, 20, 30, 40, 50, 60, 70, 80, 90, and 100% (v/v) (100% means no dilution). Ten milliliters of prepared contrast agents were placed into polyethylene centrifuge tubes (1.5 cm inner diameter, 12 cm tall, and 15 mL capacity) and were arranged in a Styrofoam rack as shown in Figure 4-2. The rack was centered in the FOV of the PET/CT scanner using lasers. For each contrast material, to minimize the effect of the location in the FOV, two scans were acquired: after the first scan, the rack was rotated 180 degrees and the second scan was obtained. CT images were obtained with the CTI-Siemens PET/CT scanners using the scanning parameter described in Chapter 3.

The images were analyzed using the scanner's software. For each tube, circular regions (37 pixels, 0.35 cm^2 area) were drawn in three places, at the top, middle, and bottom of each object, and the mean CT value for each region was recorded.

- **Experiment 2**

Gastroview™ and Omnipaque 300™ were prepared in a series of dilutions of 0, 1, 4, 10, 20, 30, 40, 50, 60, 80, and 100% (v/v) as explained in Experiment 1.

A 1.0 mL volume of diluted contrast material was pipetted into 1.5 mL polyethylene micro-centrifuge tubes (0.9 cm inner diameter), and arranged in a micro-centrifuge rack. The tubes were arranged in columns spaced at 2.4 cm, 4.0 cm, and 5.6 cm from center of the rack and FOV as illustrated in Figure 4-3.

A stock solution of ^{18}F-FDG was prepared at the concentration of 109.6 μCi/mL. A 10 μL volume of ^{18}F-FDG was pipetted into the 1 mL solution in each tube (1.1 μCi/mL). Different contrast concentrations were arranged in the Z-direction because we know that the variation of the measured activity concentration is less in this direction from the experiment in section 3.1.2.

PET images were acquired on the Reveal HD scanner using the default Thoracic protocol, except the slice thickness was set to 2 mm. The image data were viewed with the PET/CT scanner software and the maximum pixel value of each object was recorded.

For comparison, images were also acquired using a GE Discovery ST PET/CT scanner (The GE Discovery ST is owned by Mary Bird Perkins Cancer Center) in the same experimental setting except the slice thickness was set to 3.75mm.

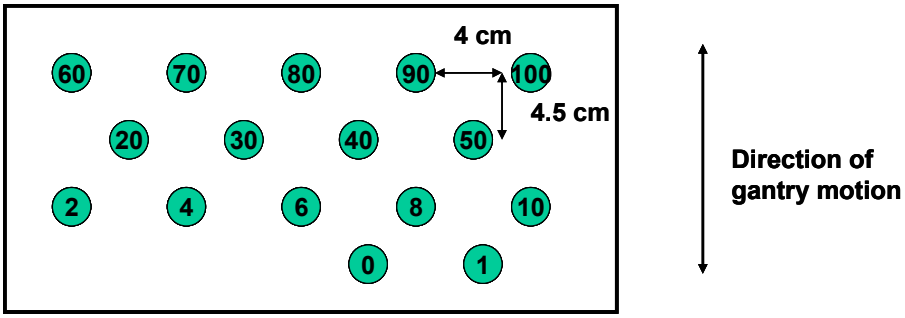

Figure 4-2: Arrangement of 15 mL centrifuge tubes. The tubes were separated 4 cm horizontally and 4.5 cm vertically. After the first scan, the arrangement was rotated 180 degree about the center of the FOV and a second scan was obtained. Numbers are dilution in % as described in the materials and methods section.

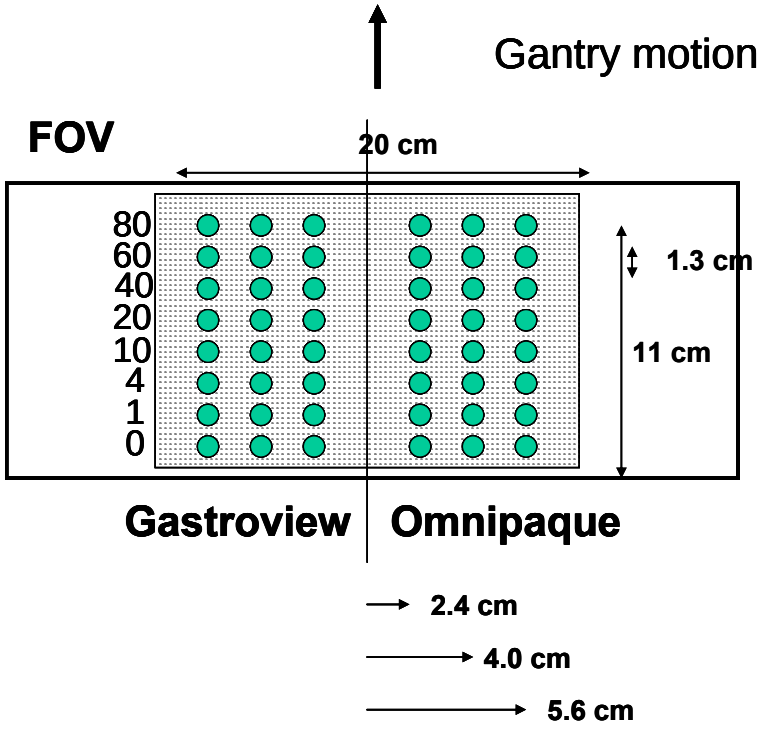

Figure 4-3: Arrangement of the micro centrifuge tubes. Numbers are dilution in % as described in Materials and Methods. Centers of the vertical columns of tubes are 2.4 cm, 4.0 cm, and 5.6 cm from the FOV center. Each row was separated by 1.3 cm.

4.2.3 Results and Discussions

- **Experiment 1**

Gastroview™ and Omnipaque 300™ demonstrated similar plots of CT values (Figure 4-4). These contrast agents contain similar organic iodine concentrations. At 3071 HU, the CT values were saturated. This is due to computer memory of CT numbers allocated, 12 bits. The typical clinical protocol uses 25 mL of Gastroview™ diluted into 240 mL of water. This yields approximately 10% on our dilution scale. The diluted Gastroview™ is administered to the patient orally about 15-30 minutes prior to an examination to allow the material to reach the pelvic bowel loop. For 2.1% barium sulfate, the CT value was lower than either iodine contrast agent for all dilutions. At 10% dilution for Gastroview™, the CT value was 822±22 HU. This is well above 300 HU where a CT number's segmentation algorithm has discontinuities, discussed in Chapter 2.2.2. The effect on the ACFs of barium sulfate, widely used in the clinical CT study, likely is negligible, because all concentrations below 70% have CT numbers less than 300 HU. Therefore, we decided to investigate only the iodine contrast materials in experiment 2.

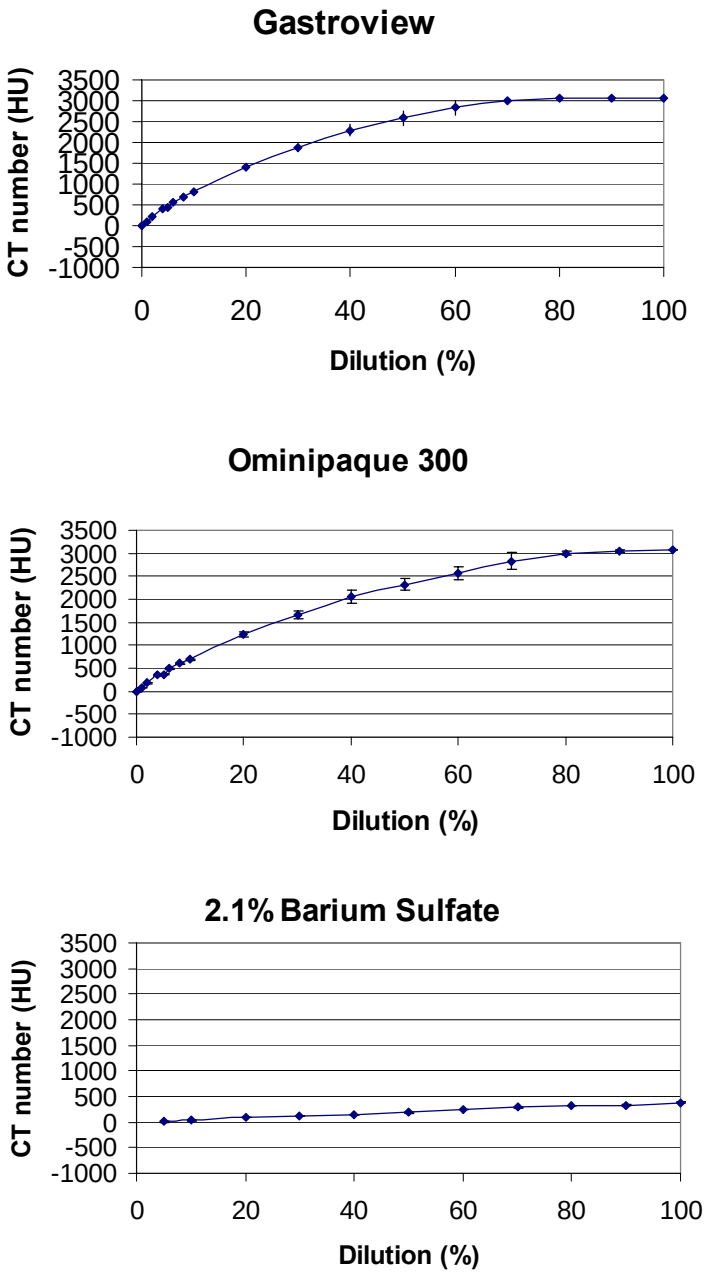

Figure 4-4: CT numbers in HU vs. concentration of contrast agents. As concentrations of Gastroview and Omnipaque increase, CT number saturates at 3,071 HU, which is near the maximum for 12 bits CT memory. The 2.1% barium sulfate dilutions span a smaller range of CT numbers and did not saturated at high concentrations.

- **Experiment 2**

The F-18 activity concentration as a function of contrast concentration is shown in Figure 4-5. For CTI/Siemens scanner, the largest error in average maximum activity concentration was seen at the highest dilution (80%). Activity concentration was overestimated 59% for Gastroview™ and 39% for Omnipaque 300™ at 80% dilution. At 10% dilution, the error was 19% and 7% respectively. At 10% dilution for Gastroview™, the clinical dose given to patient, the error in recovery in activity concentration may not be negligible. These data are consistent with our results described in Chapter 3: recovered activity concentrations are a function of position in the FOV. There are published articles using phantoms regarding contrast materials and activity concentration recoveries [17]; however no article has mentioned this variation of the activity concentration in the FOV. For a phantom study, we think radioactive materials in the FOV need to be carefully arranged to account for this variation. One problem that we did not consider at this point was distance between each row of micro-centrifuge tubes. Each row was only separated by 1.3 cm; we cannot rule out that the PET scanner resolution may cause the tube's image to overlap, altering the apparent maximum intensities. We investigate this issue in Chapter 5.

We also tested a different scanner (GE). The Discovery ST is a BGO based system (6 mm x 6 mm BGO crystals) which is larger than CTI-Siemens BGO crystals (4 mm x 4 mm)

Errors were as follows. Gastroview™: 26% for largest error at 60% dilution, 12% error for 10% dilution. Omnipaque™: 13% for largest error at 60% dilution, 5% error for 10% dilution. The GE system had less maximum error. The reason why 60% not 80%

dilution produced maximum error is unknown. We did not measure the variation of activity concentration across the FOV for this scanner. The GE scanner uses septa to acquire 2D mode data, unlike the Reveal scanner. With the different concentrations arranged in the axial direction of the gantry, it is possible that subtle differences in the position of objects in relation to the septa affect the potential sensitivity. Further investigation of the GE scanner was viewed as an extension to the primary purpose of this thesis. In the future one should investigate the effect of 2D vs. 3D acquisition modes on system response uniformity. The GE scanner is capable of retracting its septa to acquire data in 3D mode, so it would be an ideal platform for further investigation.

A recent clinical study reported that the PET artifact by an intravenous contrast material was limited to the thoracic veins containing undiluted contrast agent [36]. They also found that patients with artificially high uptake values have statistically smaller body surface area than patients with no artifacts. Another possible cause of artifacts is that bolus IV contrast passages are imaged in the CT scan but when the PET data are acquired subsequently, the high concentration of the contrast materials has redistributed throughout the body.

Another group reported that high density barium oral contrast used for some GI studies can potentially overcorrect ACFs, but the low density agent typically used for CT has negligible effects [37].

One group has investigated changes in contrast agent density with location in the GI tract. Their study used 3% gastrographin (equivalent to Gastroview) and 1.5% barium sulfate. As the oral contrast agent goes down the GI tract, the density increased: gastrographin from 143 ± 37 HU in stomach to 243 ± 43 HU in ileum; barium from

171±45 HU in stomach to 263±24 HU in ileum. They demonstrated overestimation of activity concentrations (for gastrographin 20%; barium 21%). For 50% dilution of barium, a typical concentration used in colonography, the over-estimation of activity concentration was 580% [38].

These studies indicated that if the administered volume of intravenous contrast material is corrected according to body surface area of the patient, the effect on ACFs is negligible. Barium contrast materials for gastrointestinal radiography (such as barium enema) may adversely affect ACFs for PET imaging.

Another study compared recovered activity concentrations in different organs for Ge-68 based and CT-based ACFs [39]. CT-corrected emission images showed slightly higher radioactivity concentration values for all malignant lesions and all normal organs except lung (mean 4.3% and maximum 15.2% higher). This indicates that comparison of quantitative analysis between different ACF correction methods has to be careful; one must be careful comparing SUV values among different scanners.

A

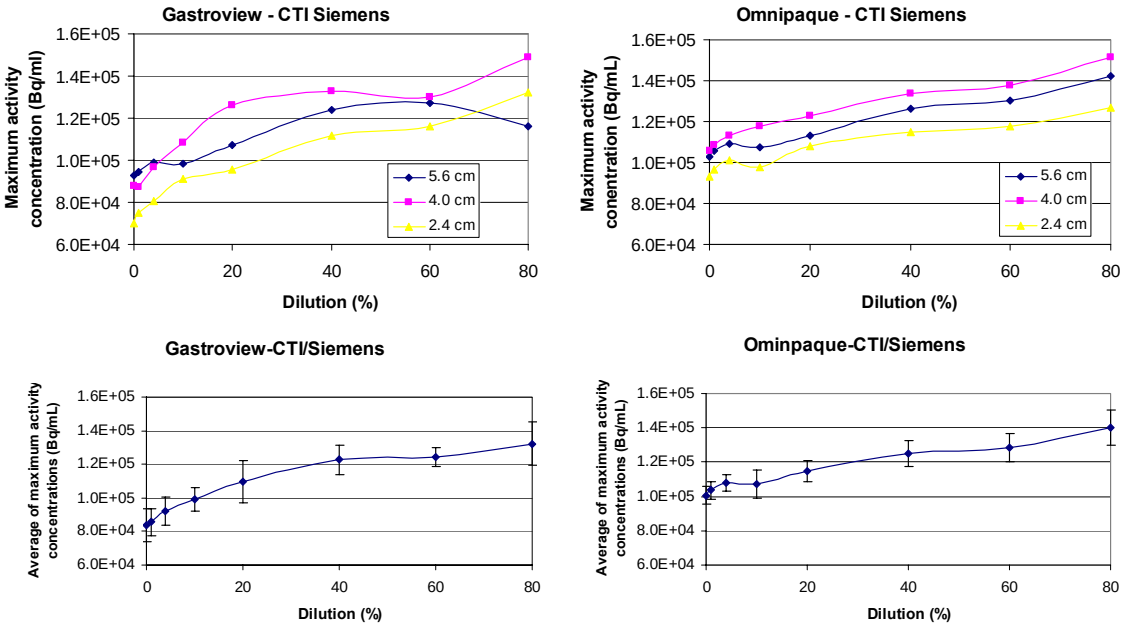

B

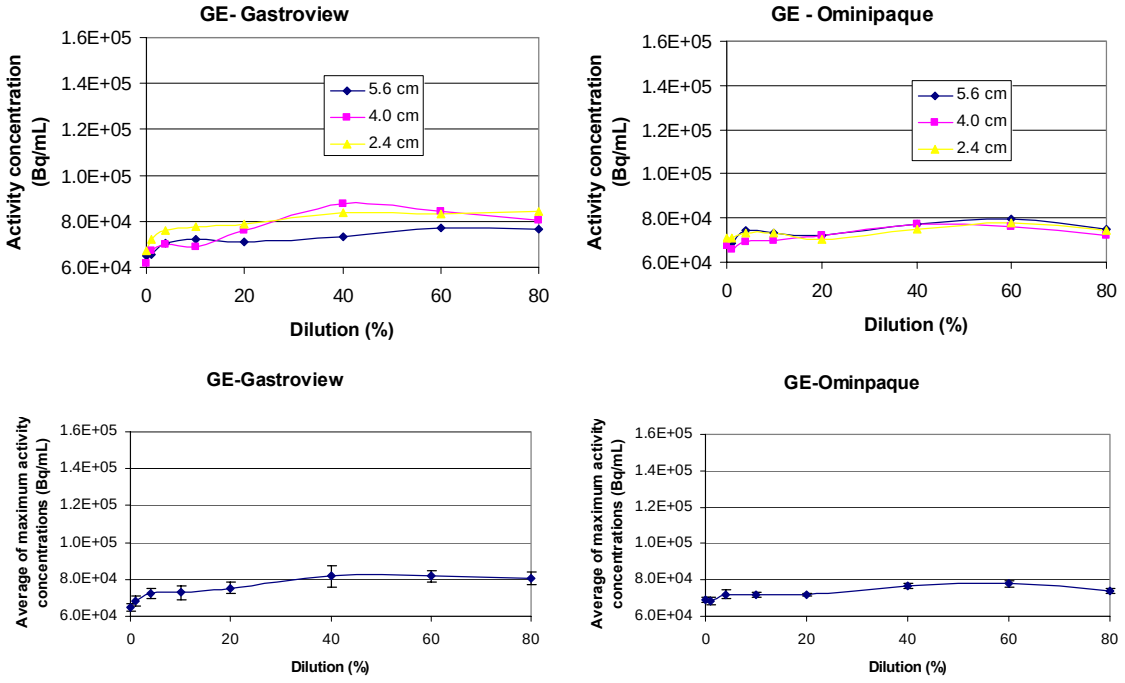

Figure 4-5: Measured activity concentration as a function of concentration of contrast agents. Two different scanners are compared (A: CTI/Siemens Reveal and B: GE Discovery). Activity concentrations for three individual distances from the center and average activity concentrations are demonstrated.

Chapter 5

Recovery of Radioactivity Concentrations of Small Spheres

5.1 Object Size and Radioactivity Concentration

5.1.1 Motivation

- **Quantitative Analysis in Oncology**

The beneficial use of the PET/CT scanner is already demonstrated in management of oncological patients in many studies. ^{18}F-FDG PET has a major impact on the management of patients with small lung cell cancer; in 29% of patients both the stage and the management was influenced by the PET results. Accurate quantitation of small lesions is especially important for diagnosis.

- **Partial Volume Effect**

In ideal quantitative PET, the image should represent the distribution of radioactive tracer concentration as a size-invariant function. Partial volume effect causes a small object, less than twice the spatial resolution of the imaging system, to have reduced signal amplitude [18, 23, 40]. This effect has been widely addressed in brain research where quantitative analysis of small areas of abnormal cortex within normal tissue is critical. If object size affects accuracy of tracer activity concentration recovery, we need to know the limitation of the method in an oncological setting. An inaccurate recovery of small lesions affects diagnosis and evaluation of the malignant lesions. Surprisingly, partial volume effects are not widely discussed in textbooks or review articles related to diagnosis of malignancy using PET/CT. Little information was found in the literature about the influence of partial volume effect on maximum pixel value measurements, such as one uses in clinical settings to calculate SUV. We tested several different sizes of spheres and sought to identify the critical object size that results in significant error in recovered activity concentration for diagnosis in the oncological setting.

5.1.2 Materials and Methods

A 0.4 μCi/mL (14800 Bq/mL) activity concentration of ^{18}F-FDG was prepared in a volume of 50 mL water. Four different diameters of plastic spheres (10 mm, 14 mm, 18 mm, and 23 mm inner diameters) were arranged on a 6 cm radius circle on the scanner's X-Z plane. The objects' centers were evenly spaced. For each diameter, three identical sizes of spheres, except for the largest 23 mm sphere, were arranged alternately and two

scans were obtained, by rotating 60 degrees around the center for each scan to minimize the effect of the location in the FOV which we discussed in Chapter 3. The routine thoracic protocol explained in the previous chapter was selected for scanning. The CT was set to 80 mA, 130 kV, and 1.0 mm slice thickness. The PET data was acquired in one PET bed for 5 minutes. The OSEM 4i8s with 128 x 128 matrix was used to reconstruct images. The maximum activity concentration (Bq/mL) of the objects in each reconstructed image was recorded. The average value was calculated from each size and the two scans.

5.1.3 Results and Discussions

The results indicate that the activity concentration error is larger, when the object diameter is smaller. The largest error of activity concentration was observed in the 10 mm sphere, which gave 46% of activity concentration of the largest sphere, as shown in Figure 5-1. The 1.4 cm sphere showed 85% of the recovered activity of the 2.3 cm sphere and the 1.8 cm sphere gave 97%. The 2.3 cm sphere gave an activity concentration of 4387 Bq/mL, compared to the expected value of 14800 Bq/mL. This error increases drastically for lesions less than 1.5 cm. The FWHM of the PET/CT scanner is approximately 7 mm. As previous publications indicated, objects less than twice the FWHM produce significant error in the activity concentration [18].

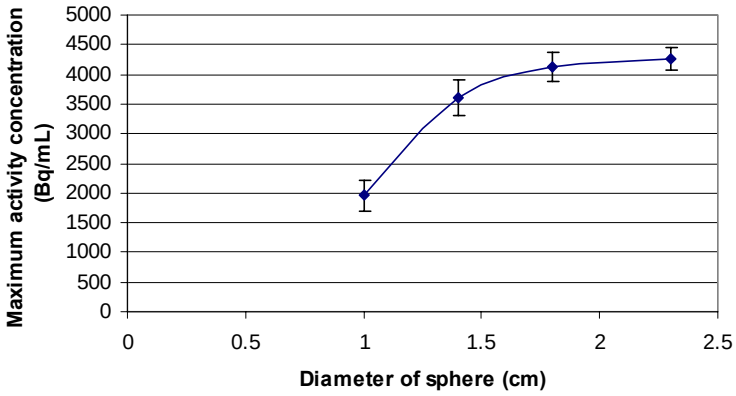

Figure 5-1: Maximum activity concentration as a function of sphere diameter. The 1.0 cm sphere recovered an activity only 46% of that recovered by the 2.3 cm sphere. Sphere less than ~1.4 cm diameter exhibit more error than larger spheres. The error bars represent standard deviation of the average of the two scans and the three spheres of each size.

According to the results, correction factors are required according to the object's size. In PET in the experimental setting, the sizes of the objects are known prior to scanning. In clinical settings, we do not know the size of the lesion in advance. However, to recover a correct activity concentration, we need an estimation of the object size. One approach is to use another imaging method, such as MRI or CT, to estimate object size. Unfortunately, small lesions may not be visible on either of these imaging methods in real practice. Some lesions visible on PET are not visible for other imaging methods. In that case, there is no way to recover the size of the object other than from PET data itself.

In an ideal situation, if the object has uniform radioactivity uptake in the lesion and if we know the point spread function of the PET image, by deconvolving the PSF from the image, we can theoretically recover an activity distribution map in the body.

If the lesion is visible on CT, then PET/CT has an advantage: the object size is available in CT data sets. Problems arise however. (1) Even normal tissue in organs

does not guarantee uniform activity distribution across patients, because there are variations among individuals. (2) Malignant lesion's uptake is not uniform for ^{18}F-FDG as we discussed in Chapter 1. Uptake reflects hypoxic cells and there are variations in uptake even within a single malignant lesion.

A literature search revealed an article discussing recovery of sphere objects [41]. Accurate quantitation of small lesions requires correction for the partial volume effects. This correction factor is called recovery coefficient (RC), and depends on the lesion size, the object-to-background ratio, and the physical properties of the object. Several approaches have been proposed to correct for partial volume effects [18, 40-42].

5.2 Radioactivity Concentration Recovery of Multiple Objects

5.2.1 Background

In the last section, we investigated the recovery size for a single object. Next, we investigated distances between objects for recovery of activity concentrations. Malignant lesions such as lymph node metastasis are sometimes located next to each other. Suppose we have recovered the correct activity concentration according to the object sizes, we still do not know if the distance between objects affects the recovery of activity concentrations.

If we place a true point source, in an ideal imaging system, the activity concentration in the image is registered as a delta function or a peak only in one pixel. However, in a real imaging system, there is a finite spread of the values. An observed image is a point spread function convolved with the distribution of the activity source.

One can imagine as two objects get close to each other, the activity concentration distributions overlap and alter the recovered values.

We chose spheres because lesions that we are interested in such as lymph nodes are generally spherical. We have tested two different sizes of three identical spheres separated in five different positions. We have also compared OSEM reconstruction to FBP reconstruction. FBP is important not only because it has minimal computational time compared to iterative algorithms, but also it is a linear analytical algorithm, ideally providing better control of the spatial resolution and noise reduction, a control necessary for quantitative data analysis [23]. We tested the FBP algorithm in different matrix sizes, and compared to OSEM to see if FBP provides more accurate activity concentration recoveries.

5.2.2 Materials and Methods

- **Experiment 1**

Three identical sizes of plastic spheres (10 mm and 18 mm inner diameter; 1 mm wall thickness) were aligned on the X axis at the center of the FOV. Outer walls of the three spheres were separated by 0 mm, 5 mm, 10 mm, 15 mm, and 20 mm (Figure 5-2) and data were acquired using the CTI-Siemens PET/CT scanner as described in Chapter 3. The activity concentration was 0.2 μCi/mL (7400 Bq/mL) and the scans used the Thorax C-A-P + C protocol. The default reconstruction algorithm (OSEM 4i8s, FORE, 128 x 128 matrix) was used to reconstruct images. Attenuation uncorrected image files formatted in DICOM was analyzed using IDL 5.6 student edition (Research System Inc., Boulder, CO). For each transaxial slice, each column was searched for the maximum pixel number and multiplied by the rescaling slope found in the DICOM file to create

maximum activity concentration profiles. The slices with the maximum activity concentration were identified. The maximum activity concentration was analyzed as a function of position in the image profiles.

- **Experiment 2**

Three spheres were positioned at the center of FOV along the X-axis. We only tested the 10 mm sphere because we already know that the 18 mm sphere gives relatively accurate recovery of activity concentration from Experiment 2 of Chapter 5.1. Three identical 10 mm plastic spheres were aligned on the X axis at the center of FOV. The outer walls of the spheres were separated by 0 mm and images were acquired with the CTI-Siemens PET/CT scanner as described in Chapter 3. The activity concentration was 0.2 μCi/mL (7400 Bq/mL). The same raw data were reconstructed three different ways into images. The methods were (a) OSEM 4i8s, FORE, 128 x 128 matrix; (b) FBP with Gaussian filter with 3mm FWHM, 128 x 128matrix; (c) FBP with Gaussian filter with 3mm FWHM, 512 x 512 matrix. Attenuation uncorrected image files formatted in DICOM were analyzed using IDL 5.6 student edition (Research System Inc., Boulder, CO). For each transaxial slice, each column was searched for the maximum pixel number to created image profiles. All trans-axial slices were examined and the slice that gave the maximum pixel numbers was selected and multiplied by the rescaling slope found in the DICOM file to calculate maximum activity concentration. Activity concentrations were analyzed as a function of position across the scanner FOV.

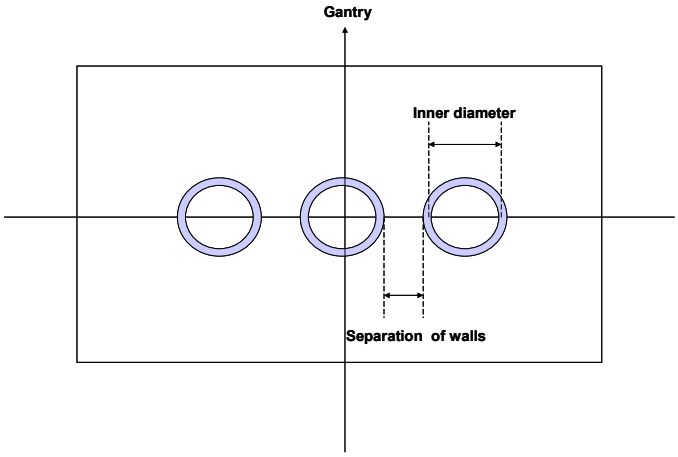

Figure 5-2: Arrangement of three identical hollow spheres. The separations of the objects were measure in separation of outer walls. The center sphere was located at the center of FOV. The three balls were arranged in tandem along the X-axis.

5.2.3 Results and Discussion

- **Experiment 1**

The results are shown in Figure 5-3. Variations in maximum activity concentrations were greater in 10 mm spheres than in 18mm spheres. This is probably due to the partial volume effect that we discussed previously. For a small object, only a small number of pixels compose its image, possibly introducing significant errors in recovery of activity concentrations. The locations of small objects relative to the pixel grid might have a large effect. Some of the variation may also be due to the location-dependent variation in uniformity described in Chapter 3. All recovered activities were less that the values prepared (7400 Bq/mL). Errors are possibly attributed to normalization process of the PET/CT scanner or dose calibration error using well counter. We did not investigate the cause of the errors at the time of experiment.

Overlaps of the images of the spheres are not as great as we expected; the amount of overlap is indicated by the profiles not reaching a value of zero. At 10 mm separation, the objects do not overlap. This is consistent with the PET resolution of 7 mm FWHM.

- **Experiment 2**

Figure 5-4 shows the results for the three different reconstruction methods. Our results indicate that increasing matrix size for FBP improves the recovery of maximum activity concentrations for the three spheres. Increased matrix size has a smoothing effect on objects (Figure 5-4). This is consistent with the results in Chapter 3 testing different matrix size with OSEM. An increase in matrix size improved the recovery of activity concentrations. We used the same raw data to reconstruct images using the three different methods. Calibrated activity concentration was 0.2 μCi/mL (7400 Bq/mL). The maximum activity concentrations were highest in OSEM 128 x 128 among all three algorithms; however it still has lower activity concentration than calibrated values. This indicates that recovered activity concentrations were not quite accurate for any method. Among the three reconstruction algorithms, 512 x 512 FBP gave less variation in maximum activity concentrations. 128 x 128 FBP gave the smallest activity concentration values. The discrepancies observed in all experiments between calibrated and recovered activity concentrations could be due to calibration errors in the well counter when measuring a small activity source. Likewise, scaling errors from counts per pixel to activity concentrations by the PET/CT scanner software also could cause the observed discrepancies.

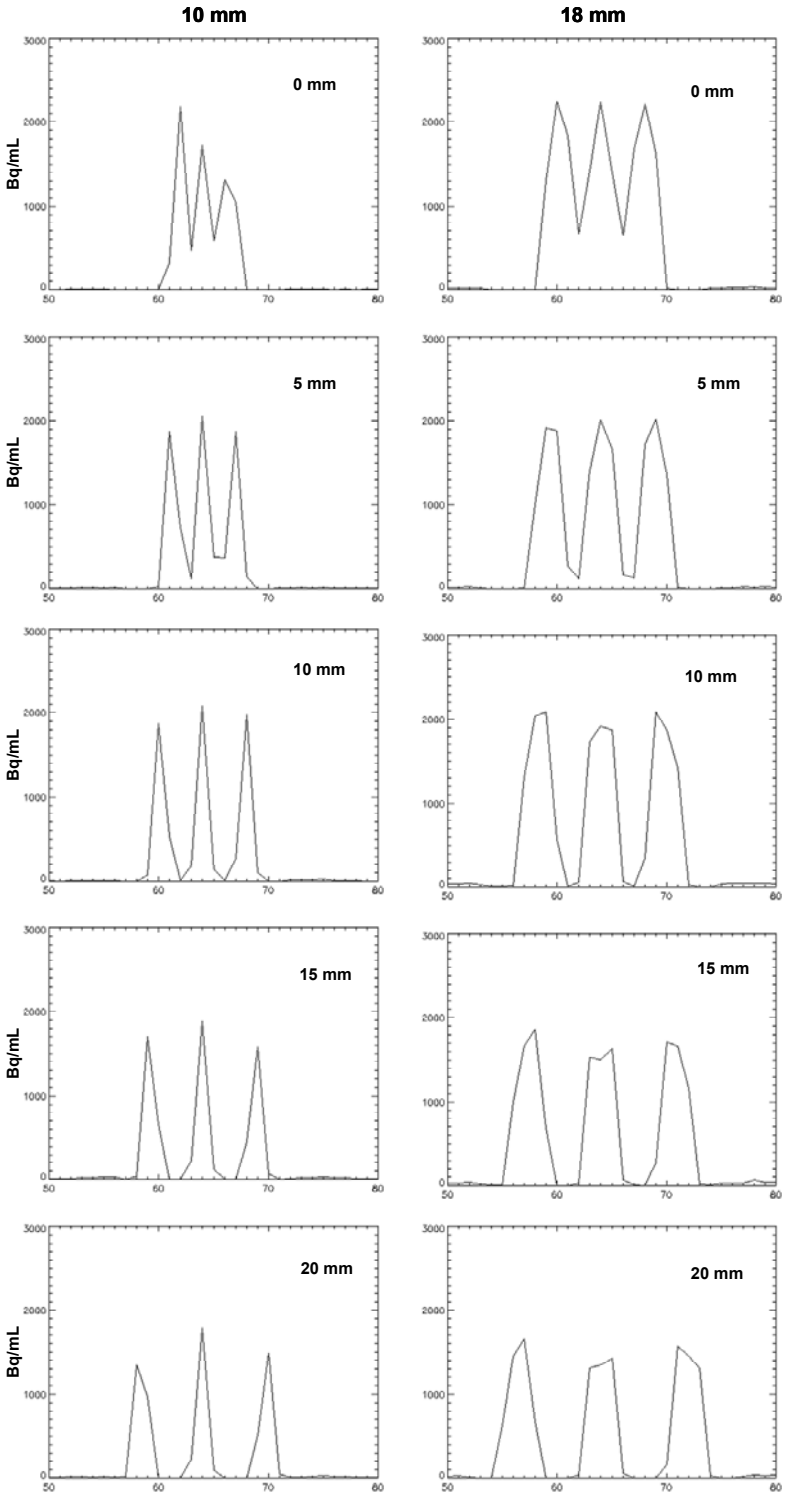

Figure 5-3: Profiles of maximum activity concentrations of three spheres arranged in tandem. 10 mm and 18 mm diameter spheres were tested. Outer walls of spheres were separated 0, 5, 10, 15, and 20 mm. Maximum pixel values were searched in Y-direction and activity concentrations were plotted a function of position along the X-axis.

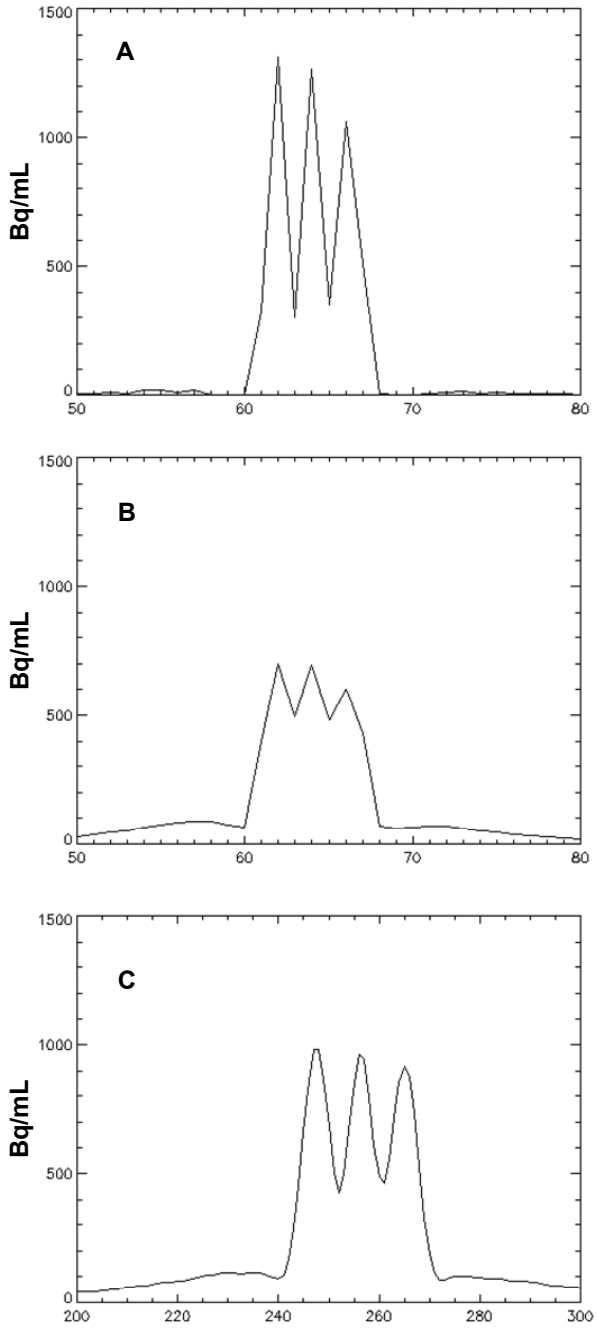

Figure 5-4: Maximum activity concentration recovery for three spheres arranged in tandem are plotted as a function of position in X-direction. Three different image reconstructions were tested on the same raw data. A: OSEM 4i8s 128 x 128matrix, B: FBP 128 x 128 matrix, and C: FBP 512 x 512 matrix. Outer walls of the spheres are spaced without any gap.

Chapter 6

Conclusions

In Chapter 3, we demonstrated that the currently available clinical PET/CT scanner does not guarantee accurate recoveries of activity concentrations with clinical scanning modes. The normalization process of the PET scanner using a continuous volume source does not lead to an accurate normalization of discrete small sources in the FOV. Also the image reconstruction parameters should be optimized by further investigations.

In Chapter 4, we tested one of the possible factors, contrast agents, that might affect quantitation of the PET/CT data. The iodine-based oral and intravenous contrast agents we tested seem to be in the range where the effects on attenuation correction factors may be negligible, except for some particular conditions discussed in that Chapter.

In Chapter 5, we demonstrated that the size of the objects affects activity concentrations; errors are not negligible for small objects less than twice the FWHM of the PET scanner. To use PET/CT as a quantitative method, an algorithm that corrects for object size variation is probably necessary. However, obtaining an accurate estimate of object size can be difficult in clinical situations. Our multiple lesion model using three spheres demonstrated the major issue is their sizes rather than separation between objects, probably because of partial volume effects. Increasing the matrix size of the reconstructed image improved the PET/CT scanner's quantitative accuracy. Immediate possible improvement of clinical PET/CT scanner is to increase matrix size of reconstruction for quantitaion purpose. . Another solution is to improve PET scanners' resolution, thereby reducing partial volume effects

A question thus arises: Suppose we could overcome all technical difficulties of recovering the activity concentration. We are still dealing with many factors involved in calculation of SUV's, such as variation in metabolism of ^{18}F-FDG among patients and variation in time elapsed between injections and scanning (although the scanners decay-correct the image data, count statistics will change). Consequently, is SUV the best choice?

It seems to be more reasonable to use an average uptake value of the organ which is unique to an individual patient and an individual scanner to distinguish malignant lesions from benign lesions. One possible calculation is

$$Ratio = \frac{Lesion\,[Bq/mL]}{Average\ Organ\,[Bq/mL]} \qquad (15)$$

$Lesion$: Activity concentration of the region of interest

Average Organ: Average activity concentration of all pixels in the specified organ

Delineation of organs and ROIs is labor-intensive. The development of automated segmentation algorithms would be helpful for this task.

A similar approach has been used in radiology. A CT scan data set has gray scale values in HU. For diagnosing different lesions in different organs, radiologists will typically look at three sets of images: bone window, soft tissue window, and lung window. The CT value is a representation of a physical property (attenuation coefficients) unique to each tissue type. These windows can be optimized manually by the radiologist; the optimal bone window may be different in health young individuals as opposed to an older individual with osteoporosis. However, each window does not vary greatly among individuals.

In ^{18}F-FDG PET, an analogous window approach is not possible. This is due to ^{18}F-FDG uptake reflecting both normal tissue and tumor physiology. The distribution of activity concentration varies from patient to patient. Given the activity concentrations of individual pixels, one cannot conclude if it is normal tissue or a malignant lesion. However, SUV value is essentially taking this approach for every patient; only the absolute magnitude is considered, rather than the magnitude in relation to surrounding organs. SUV certainly works if we have a highly-specific radioactive tracer, which exhibits no uptake in normal tissue. However ^{18}F-FDG PET with current instrumental limitations of PET scanners may not provide useful SUV values.

Well experienced nuclear medicine physicians do threholding manually to optimize display windows and they should carefully examine both attenuation-corrected and uncorrected images to visualize the lesions (Figure 6-1). However, this requires a lot of experience; a majority of physicians may not be aware of the importance of thresholding necessary for accurate diagnosis and may overlook some lesions. With the current PET/CT, with CT images' anatomical information, one can delineate organs and ROIs. CT-based delineation may help with the calculation of equation (12) and may also help to select a proper PET window. Then by comparing the activity concentration in ROI with the background concentration in particular organs, we can establish more accurate information about the lesions.

Our conclusion is: Although ^{18}F-FDG based PET/CT scanners have great advantages in radiation therapy, particularly for detecting radiotherapy-resistant hypoxic lesions, the currently available scanners are not completely satisfactory for strict quantitative analysis. Developing methods to calculate recovery coefficients for discrete sources according to size and uptake is essential to assure the quantitative quality of PET/CT in oncology settings. The development of parameters other than SUV may overcome SUV's inherent limitations reflecting the patient physiology and the scanner characteristics. We suggest that an individual organ-based PET activity concentration scale may provide for more accurate quantitation in PET/CT.

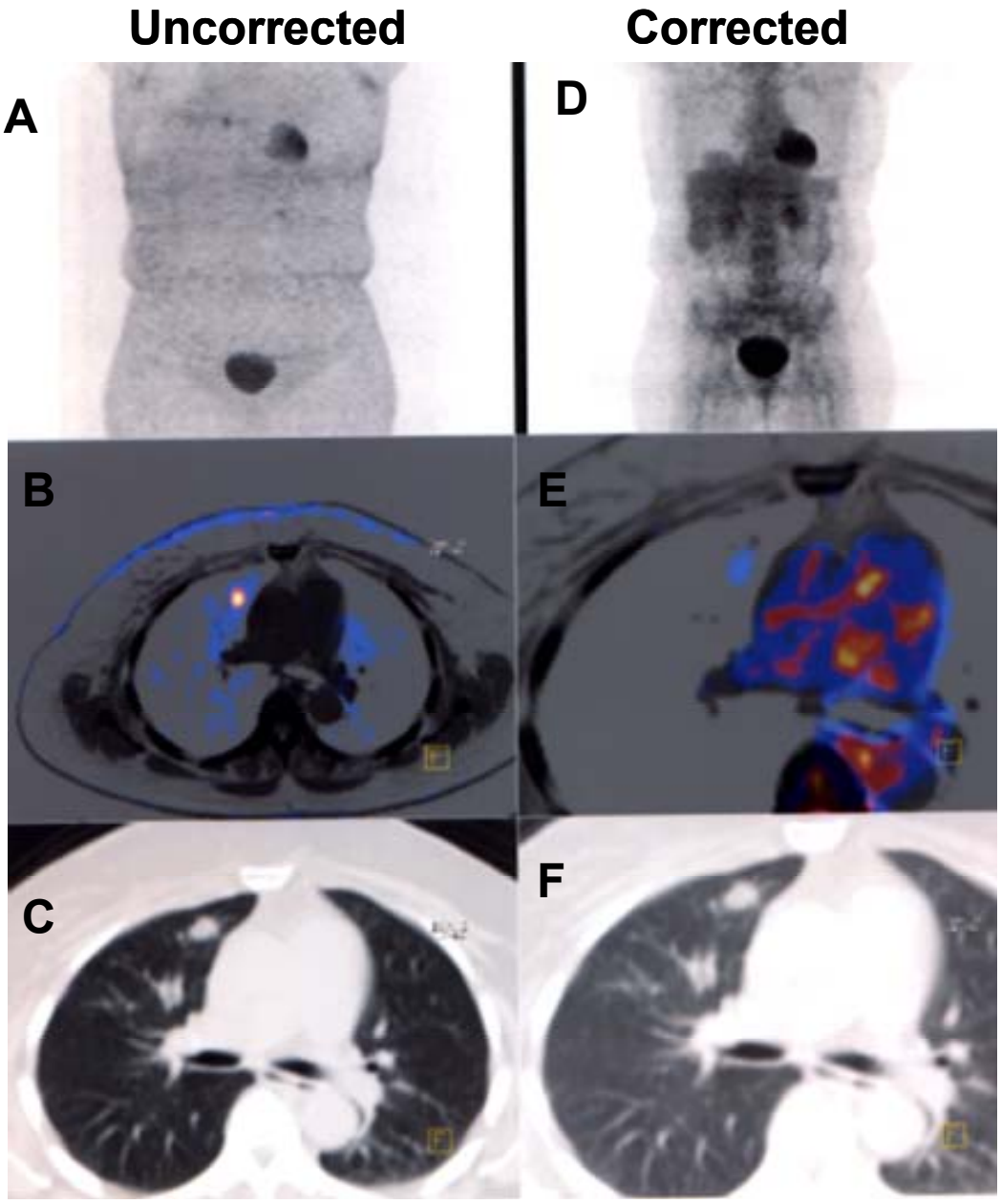

Figure 6-1: An example of the importance in optimizing display windows of both attenuation-corrected and uncorrected image sets to visualize a lesion. A-C: attenuation uncorrected image, D-F: attenuation corrected image. A lesion is visible on A, but not on D. B and E are transaxial fused PET/CT images. The lesion is easily detected on B. Only optimal windowing will allow physicians to visualize the lesion on E. C and F are transaxial CT images. The lesion is not easy to evaluate from CT images only (Courtesy of Steven Bujenovic, M.D.).

References

1. Townsend, D.W., et al., *PET/CT today and tomorrow.* J Nucl Med, 2004. **45 Suppl 1**: p. 4S-14S.

2. Townsend, D.W., T. Beyer, and T.M. Blodgett, *PET/CT scanners: a hardware approach to image fusion.* Semin Nucl Med, 2003. **33**(3): p. 193-204.

3. Lardinois, D., et al., *Staging of non-small-cell lung cancer with integrated positron-emission tomography and computed tomography.* N Engl J Med, 2003. **348**(25): p. 2500-7.

4. Kamel, E.M., et al., *Whole-body (18)F-FDG PET improves the management of patients with small cell lung cancer.* J Nucl Med, 2003. **44**(12): p. 1911-7.

5. Goerres, G.W., G.K. von Schulthess, and H.C. Steinert, *Why most PET of lung and head-and-neck cancer will be PET/CT.* J Nucl Med, 2004. **45 Suppl 1**: p. 66S-71S.

6. Mac Manus, M.P., et al., *F-18 fluorodeoxyglucose positron emission tomography staging in radical radiotherapy candidates with nonsmall cell lung carcinoma: powerful correlation with survival and high impact on treatment.* Cancer, 2001. **92**(4): p. 886-95.

7. Reed, C.E., et al., *Results of the American College of Surgeons Oncology Group Z0050 trial: the utility of positron emission tomography in staging potentially operable non-small cell lung cancer.* J Thorac Cardiovasc Surg, 2003. **126**(6): p. 1943-51.

8. Gayed, I., et al., *Comparison of bone and 2-deoxy-2-[18F]fluoro-D-glucose positron emission tomography in the evaluation of bony metastases in lung cancer.* Mol Imaging Biol, 2003. **5**(1): p. 26-31.

9. Bradley, J.D., et al., *Implementing biologic target volumes in radiation treatment planning for non-small cell lung cancer.* J Nucl Med, 2004. **45 Suppl 1**: p. 96S-101S.

10. Sharma, V., G.D. Luker, and D. Piwnica-Worms, *Molecular imaging of gene expression and protein function in vivo with PET and SPECT.* J Magn Reson Imaging, 2002. **16**(4): p. 336-51.

11. Dearling, J.L., et al., *Analysis of the regional uptake of radiolabeled deoxyglucose analogs in human tumor xenografts.* J Nucl Med, 2004. **45**(1): p. 101-7.

12. Maisey, M., R.L. Wahl, and S.F. Barrington, *Atlas of clinical positron emission tomography*. 1999, London, New York: Arnold ; Co-published in the USA by Oxford University Press. xi, 346 p.

13. Beyer, T., et al., *Acquisition protocol considerations for combined PET/CT imaging.* J Nucl Med, 2004. **45 Suppl 1**: p. 25S-35S.

14. Cohade, C. and R.L. Wahl, *Applications of positron emission tomography/computed tomography image fusion in clinical positron emission tomography-clinical use, interpretation methods, diagnostic improvements.* Semin Nucl Med, 2003. **33**(3): p. 228-37.

15. Antoch, G., et al., *To enhance or not to enhance? 18F-FDG and CT contrast agents in dual-modality 18F-FDG PET/CT.* J Nucl Med, 2004. **45 Suppl 1**: p. 56S-65S.

16. Nakamoto, Y., et al., *Effects of nonionic intravenous contrast agents at PET/CT imaging: phantom and canine studies.* Radiology, 2003. **227**(3): p. 817-24.

17. Nehmeh, S.A., et al., *Correction for oral contrast artifacts in CT attenuation-corrected PET images obtained by combined PET/CT.* J Nucl Med, 2003. **44**(12): p. 1940-4.

18. Quarantelli, M., et al., *Integrated software for the analysis of brain PET/SPECT studies with partial-volume-effect correction.* J Nucl Med, 2004. **45**(2): p. 192-201.

19. Vogel, W.V., et al., *PET/CT: panacea, redundancy, or something in between?* J Nucl Med, 2004. **45 Suppl 1**: p. 15S-24S.

20. Goerres, G.W., et al., *Accuracy of image coregistration of pulmonary lesions in patients with non-small cell lung cancer using an integrated PET/CT system.* J Nucl Med, 2002. **43**(11): p. 1469-75.

21. Nehmeh, S.A., et al., *Effect of respiratory gating on quantifying PET images of lung cancer.* J Nucl Med, 2002. **43**(7): p. 876-81.

22. Nehmeh, S.A., et al., *Reduction of respiratory motion artifacts in PET imaging of lung cancer by respiratory correlated dynamic PET: methodology and comparison with respiratory gated PET.* J Nucl Med, 2003. **44**(10): p. 1644-8.

23. Valk, P.E., *Positron emission tomography : basic science and clinical practice*. 2003, London ; New York: Springer. xix, 884 p.

24. Tarantola, G., F. Zito, and P. Gerundini, *PET instrumentation and reconstruction algorithms in whole-body applications.* J Nucl Med, 2003. **44**(5): p. 756-69.

25. Kinahan, P.E., B.H. Hasegawa, and T. Beyer, *X-ray-based attenuation correction for positron emission tomography/computed tomography scanners.* Semin Nucl Med, 2003. **33**(3): p. 166-79.

26. Turkington, T.G., *Introduction to PET instrumentation.* J Nucl Med Technol, 2001. **29**(1): p. 4-11.

27. Accorsi, R., et al., *Optimization of a fully 3D single scatter simulation algorithm for 3D PET.* Phys Med Biol, 2004. **49**(12): p. 2577-98.

28. Moses, W.W. and S.E. Derenzo, *Design studies for a PET detector module using a pin photodiode to measure depth of interaction.* IEEE Trans Nucl Sci, 1994. **41**(4): p. 1441-1445.

29. Zaidi, H., M.L. Montandon, and D.O. Slosman, *Magnetic resonance imaging-guided attenuation and scatter corrections in three-dimensional brain positron emission tomography.* Med Phys, 2003. **30**(5): p. 937-48.

30. Jain, A.K., *Fundamentals of digital image processing.* 1989, Englewood Cliffs, NJ: Prentice Hall. xxi, 569 p.

31. Barrett, H.H. and W. Swindell, *Radiological imaging : the theory of image formation, detection, and processing.* 1981, New York: Academic Press. 2 v. (xxiii, 693 p.).

32. Bushberg, J.T., *The essential physics of medical imaging.* 2nd ed. 2002, Philadelphia: Lippincott Williams & Wilkins. xvi, 933 p.

33. --, *Fludeoxyglucose F18 Injections [18F]FDG,* Biomedical Research Foundation of Northwest Louisiana: Shreveport, LA.

34. Badawi, R.D., et al., *A comparison of normalization effects on three whole-body cylindrical 3D PET systems.* Phys Med Biol, 2000. **45**(11): p. 3253-66.

35. Cohade, C., et al., *Initial experience with oral contrast in PET/CT: phantom and clinical studies.* J Nucl Med, 2003. **44**(3): p. 412-6.

36. Antoch, G., et al., *Focal tracer uptake: a potential artifact in contrast-enhanced dual-modality PET/CT scans.* J Nucl Med, 2002. **43**(10): p. 1339-42.

37. Cohade, C., et al., *Oral Contrast agent induced artifacts with PET-CT: Phantom studies and clinical case observation.* J Nucl Med, 2002. **43 Suppl.**(5): p. 308P.

38. Antoch, G., et al., *Effect of oral contrast agents on computed tomography-based positron emission tomography attenuation correction in dual-modality positron emission tomography/computed tomography imaging.* Invest Radiol, 2003. **38**(12): p. 784-9.

39. Nakamoto, Y., et al., *PET/CT: comparison of quantitative tracer uptake between germanium and CT transmission attenuation-corrected images.* J Nucl Med, 2002. **43**(9): p. 1137-43.

40. Geworski, L., et al., *Recovery correction for quantitation in emission tomography: a feasibility study.* Eur J Nucl Med, 2000. **27**(2): p. 161-9.

41. Chen, C.H., et al., *Simultaneous recovery of size and radioactivity concentration of small spheroids with PET data.* J Nucl Med, 1999. **40**(1): p. 118-30.

42. Chen, C.H., et al., *A nonlinear spatially variant object-dependent system model for prediction of partial volume effects and scatter in PET.* IEEE Trans Med Imaging, 1998. **17**(2): p. 214-27.

Vita

Yuri Ishihara was born in Kyoto, a unique historical old capital of Japan, where modern technology and Japanese tradition fuse into one. She completed her medical education at Mie University School of Medicine in1993. After graduation she entered her general surgery residency program at the Kyoto Prefectural University of Medicine and Kyoto Second Red Cross Hospital. She became a board certified surgeon of the Japanese Surgical Society in 1998. After she moved to the United States to reside in Baton Rouge, Louisiana, with her husband, she participated in biomedical research at the Pennington Biomedical Research Center as a postdoctoral research fellow under George Bray, MD and David York, PhD from 1999 to 2002 while she was enrolled in undergraduate physics courses at the Louisiana State University. In 2002, upon her award of the Board of Regents fellowship, she started her graduate study in medical physics at Louisiana State University. Her interest in medical physics is applications of medical imaging to improve safety and accuracy of surgical procedures. After graduation, she is joining to Image Guided Therapy Program at Brigham and Women's Hospital, Harvard Medical School, in Boston, Massachusetts as a fellow.